SANDIA REPORT
SAND2017-10517
Unlimited Release
Printed October 2017

Modeling Nonlinear Energy Dissipation of the Ministack Assembly

Robert J. Kuether, David A. Najera

Prepared by
Sandia National Laboratories
Albuquerque, New Mexico 87185 and Livermore, California 94550

Sandia National Laboratories is a multimission laboratory managed and operated by National Technology and Engineering Solutions of Sandia, LLC, a wholly owned subsidiary of Honeywell International, Inc., for the U.S. Department of Energy's National Nuclear Security Administration under contract DE-NA0003525.

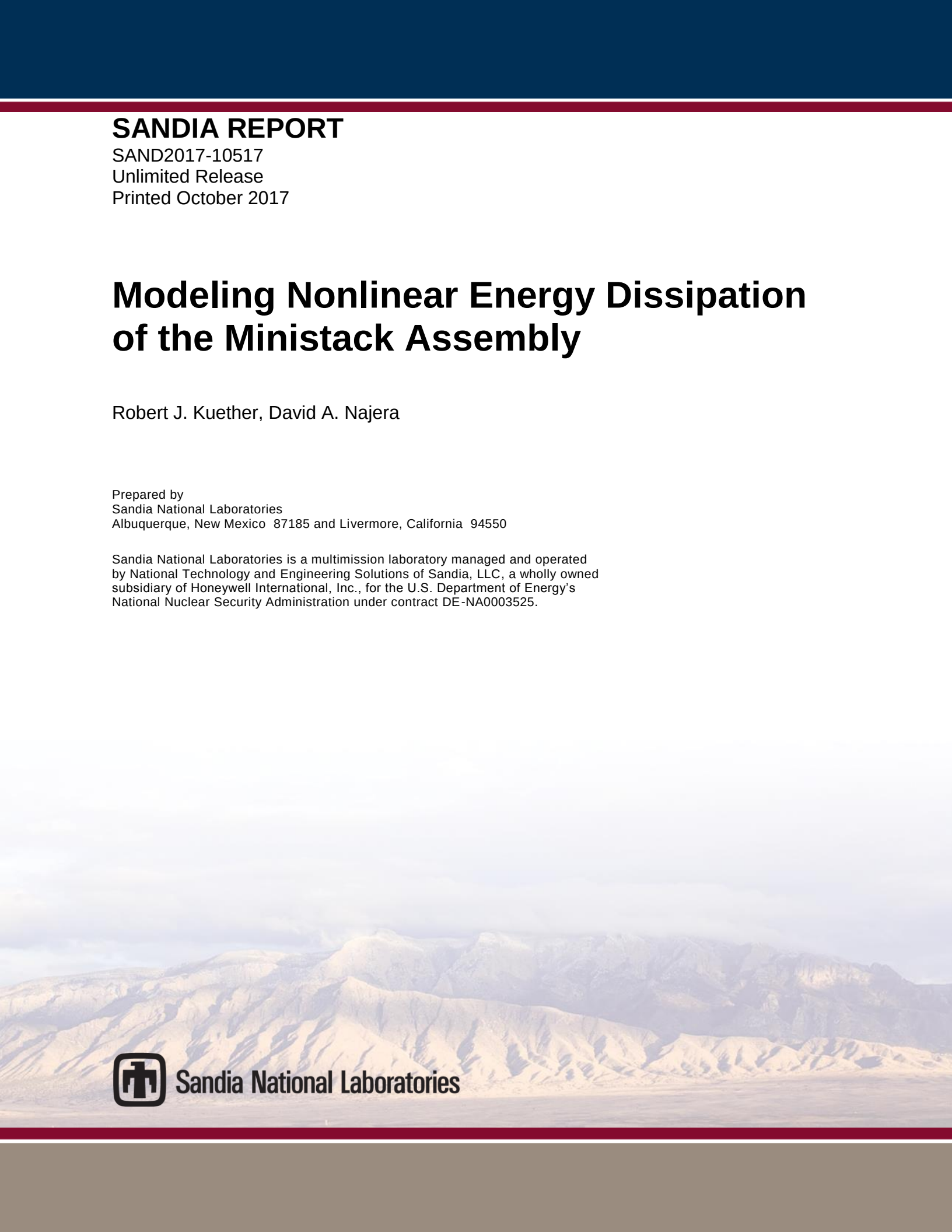

Issued by Sandia National Laboratories, operated for the United States Department of Energy by National Technology and Engineering Solutions of Sandia, LLC.

Available to DOE and DOE contractors from
U.S. Department of Energy
Office of Scientific and Technical Information
P.O. Box 62
Oak Ridge, TN 37831

Telephone: (865) 576-8401
Facsimile: (865) 576-5728
E-Mail: reports@osti.gov
Online ordering: http://www.osti.gov/scitech

Available to the public from
U.S. Department of Commerce
National Technical Information Service
5301 Shawnee Rd
Alexandria, VA 22312

Telephone: (800) 553-6847
Facsimile: (703) 605-6900
E-Mail: orders@ntis.gov
Online order: http://www.ntis.gov/search

SAND2017-10517
Printed October 2017
Unlimited Release

Modeling Nonlinear Energy Dissipation of the Ministack Assembly

Robert J. Kuether, David A. Najera
Component Science and Mechanics (Org. 01556)
Sandia National Laboratories
P. O. Box 5800
Albuquerque, New Mexico 87185-0346

Abstract

An assessment of two methodologies used at Sandia National Laboratories to model mechanical interfaces is performed on the Ministack finite element model. One method uses solid mechanics models to model contacting surfaces with Coulomb frictional contact to capture the physics. The other, termed the structural dynamics reduced order model, models the interface with a simplified whole joint model using four-parameter Iwan elements. The solid mechanics model resolves local kinematics at the interface while the simplified structural dynamics model is significantly faster to simulate. One of the current challenges to using the whole joint model is that it requires calibration to data. A novel approach is developed to calibrate the reduced structural dynamics model using data from the solid mechanics model to match the global dynamics of the system. This is achieved by calibrating to amplitude dependent frequency and damping of the system modes, which are estimated using three different approaches.

ACKNOWLEDGMENTS

The authors would like to acknowledge a number of people who helped contribute to this work. First, we would like to thank Laura Jacobs-O'Malley and John Hofer from Sandia National Laboratories for providing the experimental data on the Ministack assembly, and for discussing their observations during testing. Next, we would like to thank Matt Allen and Bob Lacayo from the University of Wisconsin-Madison for providing their codes to perform the quasi-static modal analysis. The authors appreciate the leadership and modeling feedback from Matt Brake at Rice University during the early stages of this work. The authors want to thank Scott Smith at Rice University for his help during the development of the short-time Fourier transform algorithm and applying it to experimental data to identify code issues. Finally, we would like to thank Brett Robertson and Steven Gomez at SNL for peer reviewing this report and providing helpful feedback.

TABLE OF CONTENTS

FIGURES

TABLES

NOMENCLATURE

Abbreviation	Definition
ACME	Algorithms for Contact in a Multiphysics Environment
DEAP	Distributed Evolutionary Algorithms in Python
DOF	Degrees-of-freedom
EOM	Equations-of-motion
FED	Frictional Energy Dissipation
FEA	Finite Element Analysis
HCB	Hurty/Craig-Bampton
MPC	Multi-point Constraint
NSGA-II	Non-dominated Sorting Genetic Algorithm II
QSMA	Quasi-static Modal Analysis
Sierra/SD	Sierra/Structural Dynamics
Sierra/SM	Sierra/Solid Mechanics
SNL	Sandia National Laboratories
SOM	Self-organizing Map
STFT	Short-time Fourier Transform

1. INTRODUCTION

Mechanical interfaces within structural assemblies are numerous in aerospace applications and introduce nonlinear behavior as a result of joining processes. Common types of joints include welds, bolted connections and compression fits, all of which introduce frictional contact forces between the mating surfaces. These connections have a significant influence on the dynamic response and dissipative behavior of a built-up assembly through a mechanism called microslip, which can account for up to 90% of the damping in a structure [1]. In the aerospace and defense industry, vibration mitigation in electronic and electromechanical devices can be achieved by press fitting shock and vibration sensitive components within foam packaging material. This leads to mechanical interfaces that maintain their strength with normal contact pressure and friction to resist relative slipping between surfaces. Under time varying loads, these distributed forces vary with time such that the normal pressures fluctuate and the tangential pressures may ultimately exceed slip values. The objective of this report is to assess interface modeling strategies on a benchmark structure with compression fit joints and quantify the nonlinear energy dissipation occurring during vibration.

The Ministack assembly is a benchmark specimen that was developed at Sandia National Laboratories (SNL) to better understand the nonlinear damping and stiffness of a compression fit interface. A schematic and picture of the hardware is shown below in Figure 1. The structure consists of an outer can that houses a subassembly of an aluminum slug that fits tightly in between two foam cups. The foam-slug subassembly fits into the can, and a cover plate is inserted to apply a nominal preload force. Once preloaded, the threaded ring nut is fastened to the can to maintain the compressive load on the foam-slug subassembly. The foam-to-metal interfaces are the primary source of nonlinear energy dissipation due to frictional losses when the slug vibrates within the foam packaging. A finite element model of this structure is used throughout this report to investigate modeling strategies to predict the response of the slug when the base of the can is dynamically excited. The output response of the model is post-processed with three different numerical methods to quantify the nonlinear energy dissipation and frequency due to the presence of friction forces.

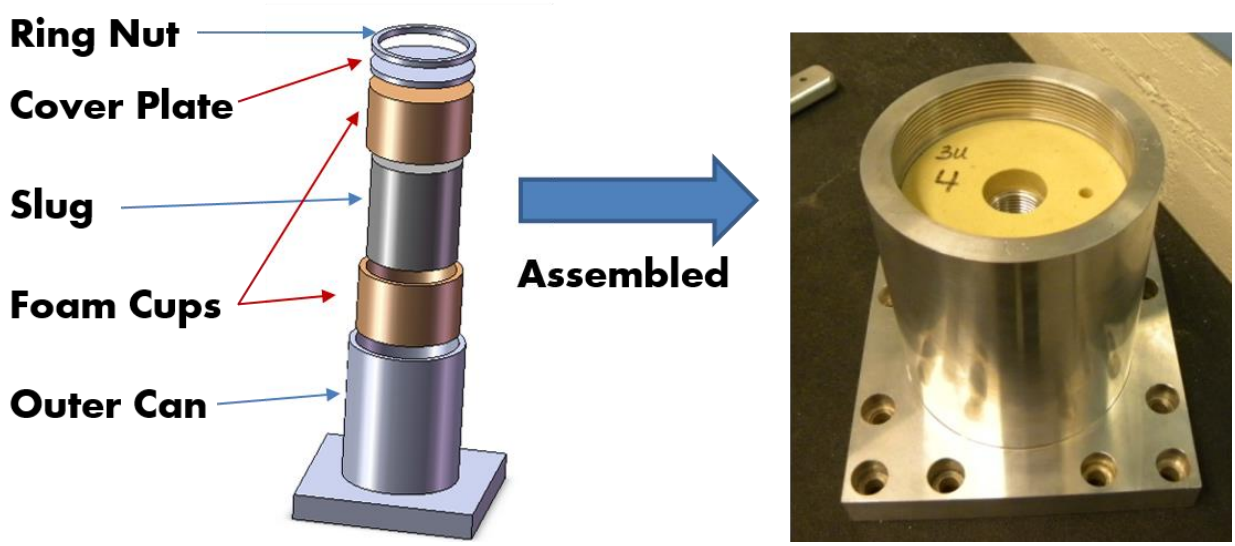

Figure 1. Ministack assembly.

A number of modeling strategies have been developed over several decades to predict the response of structures with frictional contact. Review papers by Gaul and Nitsche [2] and Bograd et al. [3] summarize various friction models that have been developed to model joint forces. The most common and readily accessible approach in industry is the finite element method. Commercially available software packages include frictional contact algorithms with both implicit and explicit solvers to predict the nonlinear response of structures with detailed geometries and complex material models. The Sierra Solid Mechanics (Sierra/SM) finite element code [4] developed at SNL is the one used throughout this work to model the Ministack in full fidelity. The drawback to using this approach is the computational cost associated with the fine mesh resolutions needed to resolve the contact forces. Simplified models of such interfaces have been developed over several decades to overcome the excessive detail needed to solve such high fidelity problems. This report utilizes the four-parameter Iwan element developed by Segalman [5], which was one of the many outcomes from a multi-year collaborative effort at SNL to better understand the response of joints under dynamic loading [6]. The Iwan element is a one-dimensional constitutive model that is a parallel arrangement of spring and slider elements with a power-law distribution describing the population density of slider element strengths. This model is used within the whole joint modeling philosophy of structural dynamics where the element forces are applied to a single node that is constrained to multiple nodes along the interface surface using multi-point constraints (MPCs). Other simplified joint models in the literature include various Iwan type elements [7, 8], Bouc-Wen hysteresis models [9, 10], and parallel Jenkins elements [2, 11].

One practical challenge associated with simplified, whole joint modeling is parameter identification of the constitutive model. Typically these functions need to be tuned to experimental or high fidelity finite element analysis (FEA) data by optimizing metrics that can be readily measured from test or output from FEA, and output from the calibration model. Examples of this include the work by Charalampakis et al. [12, 13] who developed a method to determine the parameters of a Bouc-Wen hysteretic model using different global optimization schemes. Wang et al. [14] presented a joint model updating scheme using analytical mode decomposition to extract the instantaneous characteristics of the measured and numerically integrated response. Oldfield et al. [11] fit the parameters of a Bouc-Wen and parallel Jenkins element to match the joint hysteresis predicted from a detailed finite element model. The authors of this report have recently developed an approach using a genetic algorithm implemented in [15] to calibrate the parameters of Iwan elements in the whole joint model. A multi-objective function is defined using the amplitude dependent frequency and damping from the full fidelity solid mechanics model. The whole joint structural dynamics model uses a recently developed quasi-static modal analysis technique [16] to quickly estimate the nonlinear frequency and damping, which is amenable to iterative sampling in global optimization. This approach allows the user to choose which frequency bandwidth of the structure to preserve by tailoring which modes to compare to the reference data.

Nonlinear systems and non-stationary time signals require a new set of tools for frequency domain analysis. Nonlinear signal processing tools can be used to identify how the instantaneous frequency and damping of a system changes as a function of time, or response amplitude. These amplitude dependent metrics are conceptually similar to modal damping and natural frequencies

used to characterize linear systems. Insight into this behavior helps to better understand the dynamics of a nonlinear finite element model under shock and vibration. In this report, the short-time Fourier transform (STFT) from [17] is used to estimate the instantaneous frequency and damping ratio from transient ring-down measurements due to impact excitation. The STFT takes a discrete Fourier transform over small windowed sections of the nonlinear response to estimate the frequency content at a given time instance. Similar methods based on the Hilbert transform or zero-crossing detection have been developed as well [18-22]. Sine sweep excitations of nonlinear systems have also been used to provide meaningful insight into the amplitude dependent frequency and damping while using traditional linear tools [23-25]. Recently, a quasi-static modal analysis (QSMA) technique was developed to estimate the nonlinear modal parameters [26] of a finite element model with frictional contact, and was later extended by Allen et al. [16] for whole joint models with four-parameter Iwan elements. The approach works by applying a quasi-static force in the shape of the linearized mode and computing the nonlinear response. These techniques are applied to the Ministack assembly models to evaluate the nonlinear characteristics of the structure.

The sections of this report are as follows. Section 2 briefly reviews the solid mechanics and structural dynamics modeling strategies for FEA models with nonlinear interfaces. The theory for three different methods to evaluate the amplitude dependent frequency and damping is reviewed as well. Section 3 presents a sample of test data from [27] showing the observed behavior of the Ministack assembly in the laboratory. The discussions in Section 4 pertain to the two types of numerical models developed for the Ministack, and Section 5 presents simulated results from each. Section 6 presents the model calibration study used to identify the parameters in the four-parameter Iwan element by matching the amplitude dependent frequency and damping from the solid mechanics model. The conclusions and future work are discussed in Section 7.

2. MECHANICAL INTERFACES AND NONLINEAR ENERGY DISSIPATION

2.1. Contact and Friction

The finite element models of interest are primarily linear structures containing mechanical interfaces modeled with contact and friction at a localized subset of degrees-of-freedom (DOF). Using the finite element formulation, the equations-of-motion (EOM) for the nonlinear system is written generally as,

$$\mathbf{M}\ddot{\mathbf{x}} + \mathbf{C}\dot{\mathbf{x}} + \mathbf{K}\mathbf{x} + \mathbf{f}_{NL}(\mathbf{x}, \boldsymbol{\theta}) = \mathbf{f}(t) \tag{1}$$

where $\mathbf{M}$, $\mathbf{C}$, and $\mathbf{K}$ are the $N \times N$ mass, damping, and linear stiffness matrices. The $N \times 1$ vector $\mathbf{x}$ is the displacement DOF, and the overdot represents the derivative with respect to time. The external force vector, $\mathbf{f}(t)$, describes the input to the system and the nonlinear force vector, $\mathbf{f}_{NL}(\mathbf{x}, \boldsymbol{\theta})$, contains the frictional contact forces that may depend on the internal variables of the friction element (e.g. stick or slip state). These models are developed using the Sierra/SM [4] finite element software, which is a solid mechanics code that solves frictional contact problems in addition to a variety of others, such as problems with large deformations and nonlinear material behavior. In Sierra/SM, friction can only be modeled using Coulomb behavior. However, there are several options to model contact, such as selection of the searching algorithm, the way contact is enforced, and the constraint formulations.

The contact search is performed with a proximity algorithm. The proximity algorithm generates a collection of bounding box pairs with overlapping volumes. Then, a detailed search is performed on the contact entities associated with the bounding boxes. Sierra/SM implements two searching algorithms: ACME and Dash. Their differences lie in the way the constraints are set and the contact enforcement is managed. The search method enforced depends on whether an implicit or explicit type solver is used. In general, the manual recommends using Dash because it is designed to work correctly with minimal user intervention, but the two algorithms should give the same answers if used as designed and given enough iterations during enforcement to ensure convergence.

The constraint formulation can be performed with a face-face or a node-face treatment of contact. The node-face formulation is based on the concept of preventing nodes from penetrating faces on the opposing surface pair. On the other hand, the face-face formulation prevents both faces from penetrating each other. The manual cites certain cases under which node-face contact is pathological. Some of the issues associated with node-face are remediated by the face-face formulation. Face-face is the default in Sierra/SM.

There are two basic enforcement algorithms: Kinematic and Augmented Lagrangian. The difference is in the way they achieve zero interpenetration. As the name suggests, Kinematic enforcement prescribes zero interpenetration and iterates on the forces until it is achieved. On the other hand, Augmented Lagrangian applies equal and opposite forces and iterates until zero interpenetration is obtained. The manual cites the Augmented Lagrangian as the more robust of the two algorithms as it is able to handle multiple conflicting constraints. Augmented Lagrangian is the default in Sierra/SM.

2.2. Whole Joint Models

Modeling structures with mechanical interfaces using frictional contact in Sierra/SM is as close to a "first principles" based model as one could reasonably achieve using standard finite element methods. (Note that Coulomb friction is actually an empirical model satisfying three empirical laws stating that friction is 1.) proportional to the applied load, 2.) independent of contact area, and 3.) independent of velocity.) These models have a significant computational burden associated with them, so a whole joints modeling approach is commonly used in structural dynamics to speed up time simulations. This approach condenses a mechanical interface on a linear subcomponent down to a discrete nodal location, at which a pointwise constitutive model is used to describe the behavior at the interface. This reduces the time and length scales of the joint model for time simulations requiring many steps over a long period. Detailed solid mechanics models with frictional contact require fine mesh scales not amenable to structural dynamics. The whole joint modeling philosophy relies on the assumption that the local kinematics at the interface do not significantly contribute to the response, since MPCs tie a set of nodes on the contact surface down to a single point. Figure 2 shows an example of how MPCs constrain the interface to simplify the kinematics of three bolted connections in a lap joint.

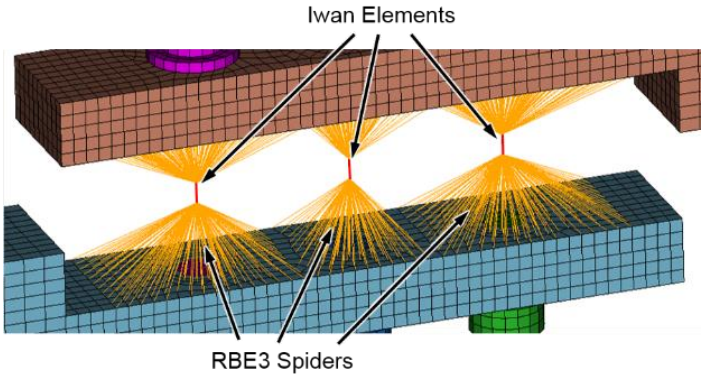

Figure 2. Example of a whole joint model of three bolts in a lap-joint [28].

It is assumed that each individual subcomponent behaves linearly (i.e. linear elastic materials, small deformations, etc..), but once assembled, the built-up structure behaviors nonlinearly due to the localized forces produced by the interface. The linear portion of the model can be reduced using the Hurty/Craig-Bampton (HCB) substructuring approach [29, 30], which reduces the linear, interior portion of the model with a truncated set of fixed-interface dynamic modes and preserves the nonlinear degrees-of-freedom at the interface with static constraint modes. Each linear subcomponent is represented with the standard HCB equations-of-motion,

$$\begin{bmatrix} \mathbf{I}_{kk} & \hat{\mathbf{M}}_{kb} \\ \hat{\mathbf{M}}_{bb} & \hat{\mathbf{M}}_{bb} \end{bmatrix} \begin{Bmatrix} \ddot{\mathbf{q}}_k \\ \ddot{\mathbf{x}}_b \end{Bmatrix} + \begin{bmatrix} \mathbf{\Lambda}_{kk} & \mathbf{0}_{kb} \\ \mathbf{0}_{bk} & \hat{\mathbf{K}}_{bb} \end{bmatrix} \begin{Bmatrix} \mathbf{q}_k \\ \mathbf{x}_b \end{Bmatrix} = \begin{Bmatrix} \mathbf{0} \\ \mathbf{f}(t) + \mathbf{r}(t) \end{Bmatrix} \tag{2}$$

The $N_k \times 1$ vector $\mathbf{q}_k$ represents the truncated fixed-interface modal coordinates and the $N_b \times 1$ vector $\mathbf{x}_b$ corresponds to the physical boundary DOF of the MPC constrained interface nodes. The $N_k \times N_k$ matrices $\mathbf{I}_{kk}$ and $\mathbf{\Lambda}_{kk}$ respectively correspond to the identity matrix and a matrix of fixed-interface mode natural frequencies along the diagonal. The unknown $N_b \times 1$ vector $\mathbf{r}(t)$

is added to the subcomponent equations to account for the unknown force applied at the interface between the adjacent structure(s).

Without loss of generality, assume that two subcomponents denoted with superscripts (A) and (B) are assembled by applying a nonlinear joint model, $\mathbf{f}_{NL}\left(\mathbf{x}_b, \boldsymbol{\theta}\right)$, at the physical boundary DOF, $\mathbf{x}_b$. These joint forces replace the unknown reaction force, $\mathbf{r}\left(t\right)$, resulting in the assembled equations,

$$\begin{bmatrix} \mathbf{I}_{kk}^{(A)} & \mathbf{0} & \hat{\mathbf{M}}_{kb}^{(A)} & \mathbf{0} \\ \mathbf{0} & \mathbf{I}_{kk}^{(B)} & \mathbf{0} & \hat{\mathbf{M}}_{kb}^{(B)} \\ \hat{\mathbf{M}}_{bk}^{(A)} & \mathbf{0} & \hat{\mathbf{M}}_{bb}^{(A)} & \mathbf{0} \\ \mathbf{0} & \hat{\mathbf{M}}_{bk}^{(B)} & \mathbf{0} & \hat{\mathbf{M}}_{bb}^{(B)} \end{bmatrix} \begin{Bmatrix} \ddot{\mathbf{q}}_k^{(A)} \\ \ddot{\mathbf{q}}_k^{(B)} \\ \ddot{\mathbf{x}}_b^{(A)} \\ \ddot{\mathbf{x}}_b^{(B)} \end{Bmatrix} + \begin{bmatrix} \boldsymbol{\Lambda}_{kk}^{(A)} & \mathbf{0} & \mathbf{0} & \mathbf{0} \\ \mathbf{0} & \boldsymbol{\Lambda}_{kk}^{(B)} & \mathbf{0} & \mathbf{0} \\ \mathbf{0} & \mathbf{0} & \hat{\mathbf{K}}_{bb}^{(A)} & \mathbf{0} \\ \mathbf{0} & \mathbf{0} & \mathbf{0} & \hat{\mathbf{K}}_{bb}^{(B)} \end{bmatrix} \begin{Bmatrix} \mathbf{q}_k^{(A)} \\ \mathbf{q}_k^{(B)} \\ \mathbf{x}_b^{(A)} \\ \mathbf{x}_b^{(B)} \end{Bmatrix} + \begin{Bmatrix} \mathbf{0} \\ \mathbf{0} \\ \mathbf{f}_{NL}\left(\mathbf{x}_b^{(A)}, \mathbf{x}_b^{(B)}\right) \\ -\mathbf{f}_{NL}\left(\mathbf{x}_b^{(A)}, \mathbf{x}_b^{(B)}\right) \end{Bmatrix} = \begin{Bmatrix} \mathbf{0} \\ \mathbf{0} \\ \mathbf{f}(t)^{(A)} \\ \mathbf{f}(t)^{(B)} \end{Bmatrix} \tag{3}$$

The nonlinear joint forces are generally dependent on the physical displacements, $\mathbf{x}_b$, and internal variables, $\boldsymbol{\theta}$. The constitutive equation used to model the interface is the four-parameter Iwan element that was originally derived for lap-type joints [5]. The theory is briefly reviewed here. This constitutive model captures the microslip behavior and nonlinear dependence of damping as the amplitude of the response increases, as well as a loss of stiffness. The force of a parallel-series Iwan model is written as,

$$F\left(t\right) = \int_0^\infty \rho\left(\phi\right)\left[u\left(t\right) - x\left(t,\phi\right)\right] d\phi \tag{4}$$

with the stick/slip condition definitions,

$$\dot{x}\left(t,\phi\right) = \begin{cases} \dot{u} & \text{if } \left\| u - x\left(t,\phi\right)\right\| = \phi \quad \text{and} \quad \dot{u}\left[u - x\left(t,\phi\right)\right] > 0 \\ 0 & \text{otherwise} \end{cases} \tag{5}$$

The dimensionless values, $x\left(t,\phi\right)$, are the displacement of the Jenkins elements with a slip displacement ϕ, $\rho\left(\phi\right)$ is the population density of Jenkins elements of strength ϕ, and $u\left(t\right)$ and $F\left(t\right)$ are the joint displacement and applied force, respectively. The schematic in Figure 3 shows the Iwan element as a set of Jenkins elements along with the population density and energy dissipation versus joint force.

A power-law population distribution that is terminated at a finite displacement is assumed as,

$$\rho\left(\phi\right) = R\phi^{\chi}\left[H\left(\phi\right) - H\left(\phi - \phi_{\max}\right)\right] + S\delta\left(\phi - \phi_{\max}\right) \tag{6}$$

Substituting this equation into Eq. (4), the force-displacement relationship becomes,

$$F\left(t\right) = \int_0^{\phi_{\max}} \left[u\left(t\right) - x\left(t,\phi\right)\right] R\phi^{\chi} d\phi + S\left[u\left(t\right) - x\left(t,\phi_{\max}\right)\right] \tag{7}$$

where the parameters of the Iwan element are defined as,

$$R = \left(\frac{F_s(1+\chi)}{\phi_{\max}^{\chi+2}\left(\beta + \left(\frac{\chi+1}{\chi+2}\right)\right)} \right) \tag{8}$$

$$S = \left(\frac{F_s}{\phi_{\max}}\right)\left(\frac{\beta}{\beta + \left(\frac{\chi+1}{\chi+2}\right)} \right) \tag{9}$$

$$\phi_{\max} = \left(\frac{F_s(1+\beta)}{K_T\left(\beta + \left(\frac{\chi+1}{\chi+2}\right)\right)} \right) \tag{10}$$

The Iwan element in Eq. (7) in conjunction with Eqns. (8) - (10) is completely defined by the following parameters: F_s (slip force), K_T (joint stiffness when no slip occurs), χ (exponent describing slope of force-dissipation curve), and β (shape parameter of the force-dissipation curve near transition to macroslip). As discussed in [5], these parameters are preferred since they are "measureable" quantities. The slip force can be estimated from static calculations with an assumed Coulomb friction coefficient, while the low amplitude stiffness can be estimated by performing vibration tests at low excitation levels. Determining the values for χ and β is more challenging, requiring specific harmonically loaded experiments to calibrate.

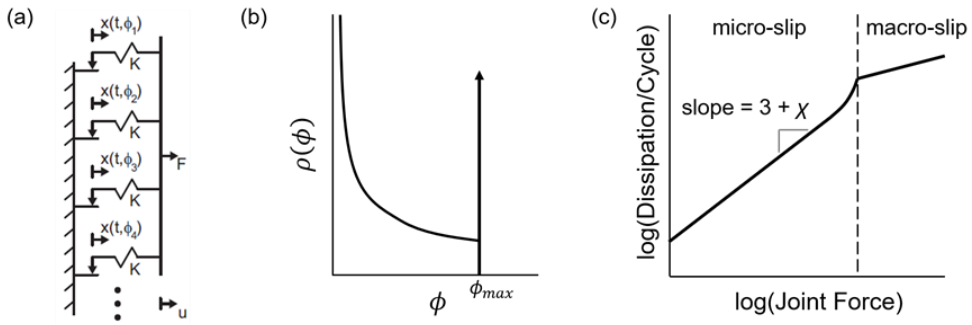

Figure 3. Schematic of the (a) parallel-series Iwan element, (b) power-law population distribution, and (c) power-law energy dissipation versus force (image from [28]).

2.3. Nonlinear Energy Dissipation

This section develops the theoretical foundation for three different methods that evaluate the nonlinear energy dissipation and stiffness of structural models with mechanical interfaces, such as the Ministack assembly that is studied later in Sections 4, 5 and 6. Each approach estimates the amplitude dependent frequency and damping of a given vibration mode using different types

of data simulated from models (i.e. Sierra/SM or whole joint model). Having numerical methods to observe and quantify the nonlinear behavior gives tremendous insight into the dynamics of the system, especially since existing nonlinear modal analysis techniques [31-33] currently do not scale to large, non-conservative models. The first method developed here is based on the short-time Fourier transform applied to ring-down response of impact loading and is a modification of the work done originally by Kuether and Brake in [17]. The second approach is based on swept sine excitation that uses traditional linear methods to estimate the frequency and damping from an approximate transfer function. The third and final approach is the quasi-static modal analysis originally developed by Festjens et al. [26] and later extended by Allen et al. [16].

2.3.1. Time-Frequency Analysis

The short-time Fourier transform operates on the freely decaying time signal of a nonlinear system, denoted as $x(t)$, measured over a period, *T*. The signal is sampled at *M* evenly spaced points in time such that the increment is defined as $\Delta = T/M$, resulting in *M* discrete measurements. Mathematically, the continuous STFT is calculated as,

$$X_{\delta}^{b}(\omega) = \int_{-\infty}^{\infty} x(t) w_{\delta}^{b}(t) e^{-i\omega t} dt \tag{11}$$

where

$$w_{\delta}^{b}(t) = w\left(\frac{t-b}{\delta}\right) \tag{12}$$

A window function, $w(t)$, moves along the time axis at time shifts, *b*, and has a much shorter time period than the measurement period, *T*, which is controlled by the dilation parameter δ. The window period should sufficiently capture several cycles of the frequency of interest. The time point *b* controls the center time of the window, allowing a Fourier transform to be taken from different sections of the signal.

One of the issues with the STFT is that the period of the window function dictates the accuracy and resolution of the spectrum. For example, if the window period is too large, then the frequency of the signal will be poorly averaged. Conversely, if the window is too small, then the poor frequency resolution makes it difficult to approximate the instantaneous frequency. In an effort to improve this, the STFT is modified to allow for the time period of the window to change as it moves down the time axis, making the dilation parameter, $\delta(b)$, dependent on the time shift, *b*. This ability to either expand or contract the window size helps produce a STFT with better averaging and resolution for frequencies that change significantly throughout the signal. The window of the STFT is modified from Eq. (12) to become

$$w_{\delta}^{b}(t) = w\left(\frac{t-b}{\delta(b)}\right) \tag{13}$$

Unlike the Fourier transform, the STFT is a two-dimensional spectrum that changes as the window moves in time. The moving window is zero-padded to improve the frequency resolution, but this does not actually improve on the estimation of the Fourier coefficients. A variety of window functions, $w(t)$, could be applied (e.g. Rectangle, Hamming, etc..) depending on the

application of interest. From experience, the authors have found that the Hanning window offered the best results for transient ring-down data, and is used throughout this report. The function for the time varying Hanning window is given as,

$$w(t)=\begin{cases}\frac{1}{2}\left(1-\cos(\pi t)\right) & 0\le t<T_w\\ 0 & otherwise\end{cases} \tag{14}$$

The period of the Hanning window, T_w, depends on the dilation parameter, δ, allowing for the period to expand or contract as the window moves position. An example of this is shown in Figure 4, where three Hanning windows expand linearly, exponentially, or remain constant (the constant window length is the original STFT). These linearly and exponentially expanding windows cover a 1.0 sec signal, with initial and final periods of 0.2 sec and 0.4 sec, respectively. They are discretized over six evenly spaced intervals between the initial and final window center times. The constant window has six windowed sections with a period length of 0.2 sec defined over a 1.0 sec period. These linear and exponentially varying windows parameters would be used for signals that decrease in frequency as time increases (or energy decreases). The variable window gives more flexibility when analyzing non-stationary signals, and results in a better estimate of the instantaneous frequency content than using constant window lengths.

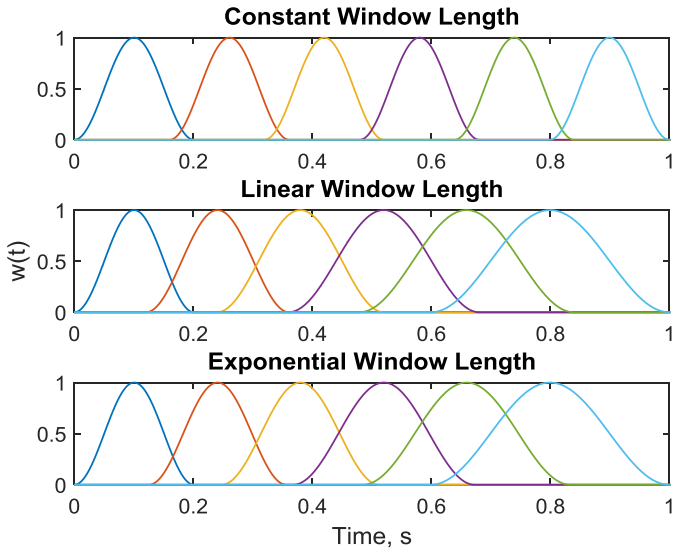

Figure 4. Three different varying window length functions for the modified STFT algorithm.

The transient ring-down response, $x(t)$, can be generally represented as a summation of decaying harmonic functions of the form,

$$x(t)=\sum_{r=1}^{p}\mathrm{Re}\left\{A_{r,0}e^{-\beta_r(t)t}e^{i\phi_r(t)}\right\} \tag{15}$$

The assumed form of the signal has a total of p decaying harmonic functions each having an initial complex amplitude, $A_{r,0}$, time dependent decay rate, $\beta_r(t)$, and time dependent phase,

$\phi_r(t)$. Time-frequency analyses such as the modified STFT described above are needed to identify the time dependency of the phase and decay rate. Following the approach in [22], the decay rate and phase are rewritten as,

$$\beta_r(t) = \zeta_r(t)\omega_r(t) \tag{16}$$

$$\phi_r(t) = \omega_{r,D}(t) \cdot t \tag{17}$$

In keeping notation with the free response of an underdamped, linear oscillator, the decaying harmonic functions are described by a time dependent damping ratio, $\zeta_r(t)$, and damped and undamped natural frequencies $\omega_{r,D}(t)$ and $\omega_r(t)$, respectively. Substituting Eqns. (16) and (17) into Eq. (15) would produce a form similar to the linear solution. The time dependent frequencies and damping ratios are estimated from the STFT data using peak picking methods to find the resonant point in the spectrum.

Now the frequency, $\omega_r(t)$, and damping, $\zeta_r(t)$, for the rth decaying harmonic function in Eq. (15) must be fit to the STFT data. Starting with the collection of Fourier coefficients in Eq. (11) with an arbitrary center time, b_i, the maximum amplitude of $X^{b_i}_{\delta(b_i)}(\omega)$ is found within a subset of frequencies [ω_{low}, ω_{high}]. The maximum amplitude of the Fourier coefficient is determined mathematically as,

$$A_r(b_i) = \max_{\omega \in [\omega_{low} \quad \omega_{high}]} \left(\left| X^{b_i}_{\delta(b_i)}(\omega) \right| \right) \tag{18}$$

and the damped frequency at the peak is denoted as $\omega_{r,D}(b_i)$.

Taking the magnitude of the rth decaying harmonic function, $A_r(b_i)$ is related to the slow-decay at window time, b_i, as,

$$A_r(b_i) = \left| A_{r,0} \right| e^{-\beta_r(b_i) b_i} \tag{19}$$

This equation alone does not uniquely solve for all unknown values of $|A_{r,0}|$ and $\beta_r(b_i)$. Assuming subsequent windows are closely spaced, the unknowns can be estimated by finding the slope between two data points with the following algebraic equation,

$$\begin{bmatrix} 1 & b_i \\ 1 & b_{i+1} \end{bmatrix} \begin{Bmatrix} \ln\left(\left| A_{r,0} \right| \right) \\ -\beta_r \end{Bmatrix} = \begin{Bmatrix} A_r(b_i) \\ A_r(b_{i+1}) \end{Bmatrix} \tag{20}$$

If the damping is sufficiently small such that $\sqrt{1-\zeta_r(b_i)^2} \approx 1$, then the damped natural frequency well approximates the undamped frequency as $\omega_{r,D}(b_i) = \omega_r(b_i)\sqrt{1-\zeta_r(b_i)^2} \approx \omega_r(b_i)$. Then, the damping ratio becomes,

$$\zeta_r(b_i) = \frac{-\beta_r}{\omega_r(b_i)} \tag{21}$$

The collection of $A_r(b)$, $\zeta_r(b)$ and $\omega_r(b)$ describe the amplitude dependent damping and frequency obtained from the measured ring-down response, $x(t)$. It should be noted that a band-pass filter may be needed to separate frequency content when multiple modes are excited at one time.

2.3.2. Resonant Peak from Base Excitation Sine Sweeps

Swept sine excitation is another approach that is most commonly used in experiment to determine the resonant peaks within a given frequency range of interest. The input is typically applied to the nonlinear structure either by applying a force or base acceleration. Assuming the latter, the acceleration of the base sweeping from ω_1 to ω_2 at a linear rate ω_{rate} is expressed as,

$$a_{base}(t) = A_0 \sin\left(\frac{1}{2}\omega_{rate}t^2 + \omega_1 t\right) \tag{22}$$

where

$$\omega_{rate} = \frac{\omega_2 - \omega_1}{T_{sweep}} \tag{23}$$

The period, T_{sweep}, dictates how long it takes for the signal to sweep between the frequency bounds ω_1 and ω_2, and the acceleration amplitude is denoted as, A_0. Typically a slower sweep rate produces better resolution of the response near resonance, but this is challenging when applied to finite element models since the increased simulation time increases computational burden. The accelerations measured at a location on the model, denoted as $a(t)$, is transformed to the frequency domain using the Fourier transform, expressed in continuous form as,

$$A(\omega) = \int_{-\infty}^{\infty} a(t)e^{-i\omega t}dt \tag{24}$$

Using the response and input accelerations in the frequency domain, $A(\omega)$ and $A_{base}(\omega)$, respectively, the transfer function is estimated as $H(\omega) = A(\omega)/A_{base}(\omega)$. From this, the resonant frequency for a given excitation amplitude, A_0, is the frequency at which the phase between the input and output is equal to -π/2. Mathematically, the natural frequency, ω_r, is the frequency at which,

$$\arg(H(\omega)) = \frac{-\pi}{2} \tag{25}$$

The damping ratio at the resonant peak is then estimated by modifying the equation from [34],

$$\zeta_r(|A(\omega_r)|) = \frac{A(\omega = 0)}{2A(\omega = \omega_r)} \tag{26}$$

When swept sine excitation is applied at various input levels, the resonant frequencies and damping ratios change as a function of the response amplitude. From this collection of data, the amplitude dependent frequency, $\omega_r(|A(\omega_r)|)$, and damping, $\zeta_r(|A(\omega_r)|)$, can be obtained for a given mode of interest.

2.3.3. Quasi-Static Modal Analysis

The recently developed quasi-static modal analysis approach shows promise as an efficient method to estimate the amplitude dependent frequency and damping without the need to run transient simulations and rely on post-processing algorithms applied to time histories. This approach is amenable to modeling but would be impossible to apply experimentally. The approach starts from the nonlinear equations-of-motion,

$$\mathbf{M}\ddot{\mathbf{x}} + \mathbf{C}\dot{\mathbf{x}} + \mathbf{K}\mathbf{x} + \mathbf{f}_{NL}(\mathbf{x}, \theta) = \mathbf{f}(t) \tag{27}$$

Note that these equations could represent either the full fidelity Sierra/SM model, or the whole joint reduced model. The quasi-static equations are obtained by ignoring the mass and damping terms,

$$\mathbf{K}\mathbf{x} + \mathbf{f}_{NL}(\mathbf{x}, \theta) = \mathbf{f}_{preload} \tag{28}$$

The preloaded displacement, $\mathbf{x}_{preload}$, is solved directly from this equation using an appropriate nonlinear static solver. The nonlinear forces are linearized about the preloaded deformation in order to approximate the linear modes of the structure. The eigenvalue problem for the modal solution is solved as,

$$\left(\mathbf{K} + \left. \frac{d\mathbf{f}_{nl}(\mathbf{x}, \theta)}{d\mathbf{x}} \right|_{\mathbf{x}=\mathbf{x}_{preload}} - \omega_r^2 \mathbf{M} \right) \boldsymbol{\varphi}_r = \mathbf{0} \tag{29}$$

where $\boldsymbol{\varphi}_r$ is the rth mode shape vector and ω_r is the corresponding natural frequency. A force vector proportional to the rth mode shape is determined to statically excite the mode of interest if the model were assumed to be linear. This force is scaled with amplitude, α, such that,

$$\mathbf{f}_{static} = \mathbf{M}\boldsymbol{\varphi}_r \alpha \tag{30}$$

This force is applied to Eq. (28) such that the right hand side becomes $\mathbf{f}_{preload} + \mathbf{f}_{static}$, and the response for a given forcing amplitude, $\mathbf{x}(\alpha)$, is modally filtered to the rth mode using $q_r(\alpha) = \boldsymbol{\varphi}_r^{\mathrm{T}} \mathbf{M}\mathbf{x}(\alpha)$. Following the approach in [16], the natural frequency is approximated using the secant of the hysteresis curve,

$$\omega_r(\alpha) = \sqrt{\alpha / q_r(\alpha)} \tag{31}$$

The damping ratio becomes,

$$\zeta_r(\alpha) = \frac{D(\alpha)}{2\pi (q_r(\alpha)\omega_r(\alpha))^2} \tag{32}$$

where the energy dissipated is determined using Masing's rules [16],

$$D(\alpha) = 2 \int_{-q_r(\alpha)}^{q_r(\alpha)} \left(f_r\left(\frac{q_r + q_r(\alpha)}{2} \right) + f_r\left(\frac{q_r(\alpha) - q_r}{2} \right) - \alpha \right) dq_r \tag{33}$$

This approach is applicable to solid mechanics models with frictional contact, as well as the reduced HCB models with four-parameter Iwan elements at the interface DOF.

3. MINISTACK ASSEMBLY HARDWARE AND EXPERIMENTAL MEASUREMENTS

The system studied in this report is termed the Ministack assembly which consists of a solid aluminum 6061-T6 mass that fits into two 20 pounds per cubic foot closed cell PMDI foam cups. This subassembly is inserted into an aluminum can, with a steel disk covering the top of the foam holding a nominal 700 pound-force preload held in place with a threaded steel ring. A schematic of the setup is shown below in Figure 5. For reference, the solid aluminum mass (i.e. slug) is 4 inches high with a diameter of 3 inches. The foam cups each have an average inner depth of 2 inches, with an average inner diameter of 2.99 inches. As a result, the slug nominally fits tightly within the foam casing allowing for the preload to go through both the foam cups and the aluminum slug. In axial base excitation, the axial mode of the slug is expected to exercise the large foam-to-metal interface between the slug, can and foam cups. This is expected to be the main source of nonlinear behavior. The axial mode of the linear structure computed from FEA is shown in Figure 6.

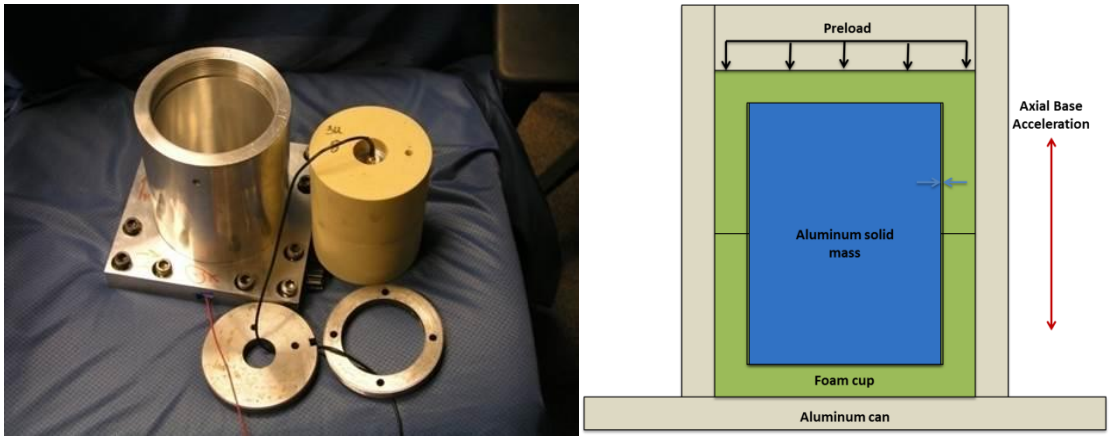

Figure 5. Ministack hardware.

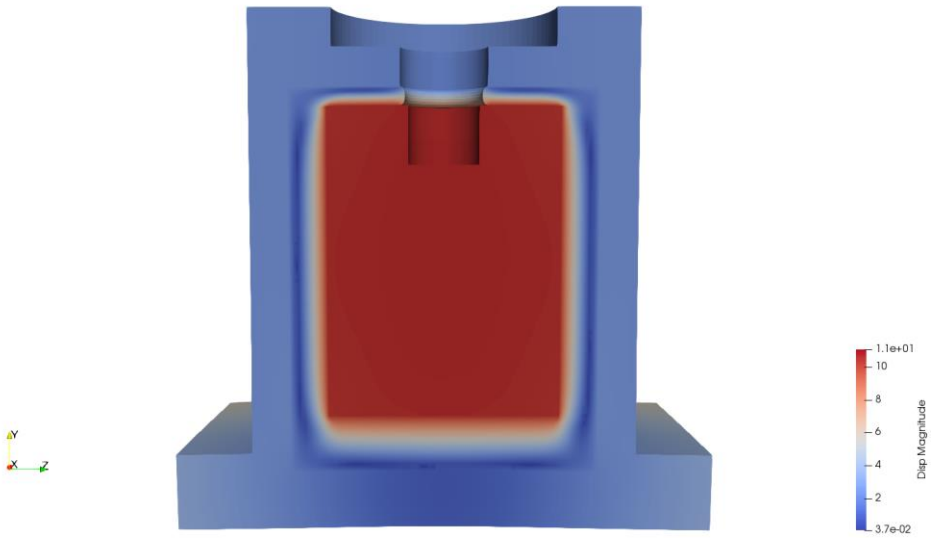

Figure 6. Axial slug mode of Ministack.

The Ministack hardware was originally developed as a benchmark system to collect experimental measurements and observe nonlinear behavior related to the energy losses at the foam-to-metal frictional interfaces. The objective was to perform sine sweeps with base excitation to excite the axial mode of the slug oscillating within the preloaded foam encapsulant. Jacobs-O'Malley and Hofer [27] recently published a SAND report documenting test results from a number of Ministack configurations, including various foam cup geometries, preload forces, slug diameters and input amplitudes. Each of these variables showed to influence the resonant frequency and damping. The report shows that the benchmark structure exhibits a large amount of assembly-to-assembly variation, as well as significant nonlinearity. A selection of the test data is summarized here to show the observed nonlinear behavior due to base excitations at increasing levels. During the tests, a uniaxial control accelerometer was placed in a recess at the bottom of the can, and a triaxial accelerometer was attached on top of the slug (as seen in the left of Figure 5). A series of sine sweep tests were carried out at various excitation levels to observe the nonlinear behavior near the resonance of the axial mode of interest. The test series is given below in Table 1.

Table 1. Sine sweep test series for Ministack assembly.

Test ID	Sweep Series Amplitudes
1	1g up, 1g down, 1g up, 1g down, 1g up, 1g
2	2g up, 2g down
3	5g up, 5g down
4	10g up, 10g down

Prior to testing, the Ministack was assembled by applying a preload with a press until the reading on the load cell was approximately 700 pounds-force. The retaining ring was tightened to maintain the preload, the press was released, and the Ministack was then bolted to the shaker. The base plate of the can was accelerated with a swept sine input between 700 and 2500 Hz at a linear rate. The first test was swept at 1 g amplitude from 700 to 2500 Hz (up), followed by a 1 g sweep from 2500 to 700 Hz (down). This was repeated two more times at a 1 g load level to allow the slug to "settle" within the foam cups. Following the 1 g sweeps, the Ministack was excited from 700 to 2500 Hz at a 2 g level, and then back down from 2500 to 700 Hz. The same upward and downward tests were then run at 5 g and 10 g levels, and the hardware was disassembled and reassembled, carefully noting the alignment as not to change the orientation of the components. The same tests were repeated for the reassembled hardware in order to observe any variability between two assembly processes.

The axial slug acceleration measured with the triaxial accelerometer was processed using the short-time Fourier transform to estimate the envelope of the signal in the frequency domain. These results are shown below in Figure 7 for all the downward sweeps (the 1 g sweep was the last of the three in the test series). There seemed to be some slight directional dependence of the sweep frequency (not shown here) but for the most part the upward and downward sweeps showed reasonably similar responses. The envelopes of the response show that as the amplitude of the base acceleration increased, the resonant frequency decreased. This is consistent with the nonlinear slip behavior in press fitted interfaces.

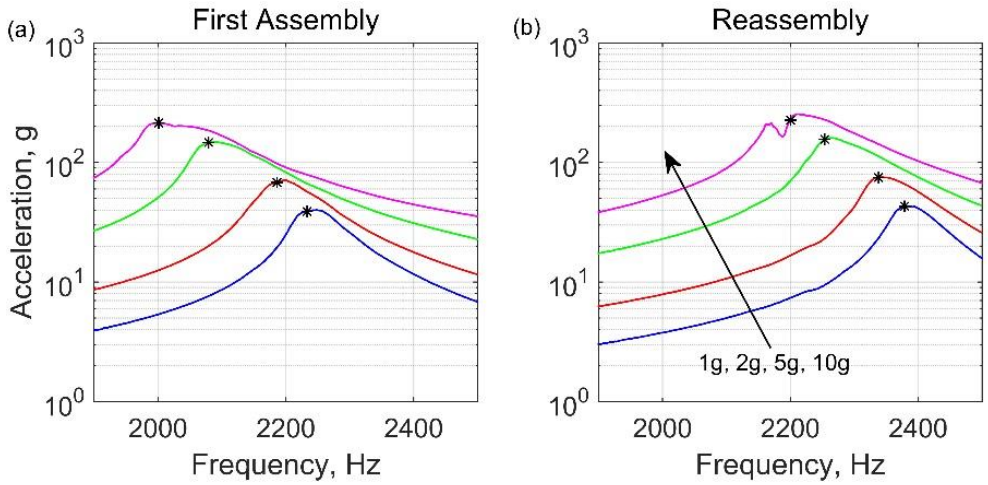

Figure 7. Swept sine response envelopes for (left) initial assembly and (right) disassembly + reassembly.

The plots in Figure 8 show the amplitude dependent frequency and damping ratio from the sine sweep data in Figure 7. The resonant frequencies were determined from the data by identifying the frequency at which the input and response were 90 degrees out-of-phase from one another. The effective damping was estimated via the half power bandwidth rule. The test data provides a qualitative reference as to how the models developed in the following sections are expected to perform under similar loading scenarios. When comparing the first assembly versus reassembly, it is interesting to note that the trends in amplitude dependent frequency and damping are similar but seemingly offset. Explaining this assembly-to-assembly variation is beyond the scope of this work, although it plays an important role in analyzing such systems. A number of physical explanations that could be responsible include material relaxation, inaccuracy of the precise preload value, or the load path within the assembly, to name a few.

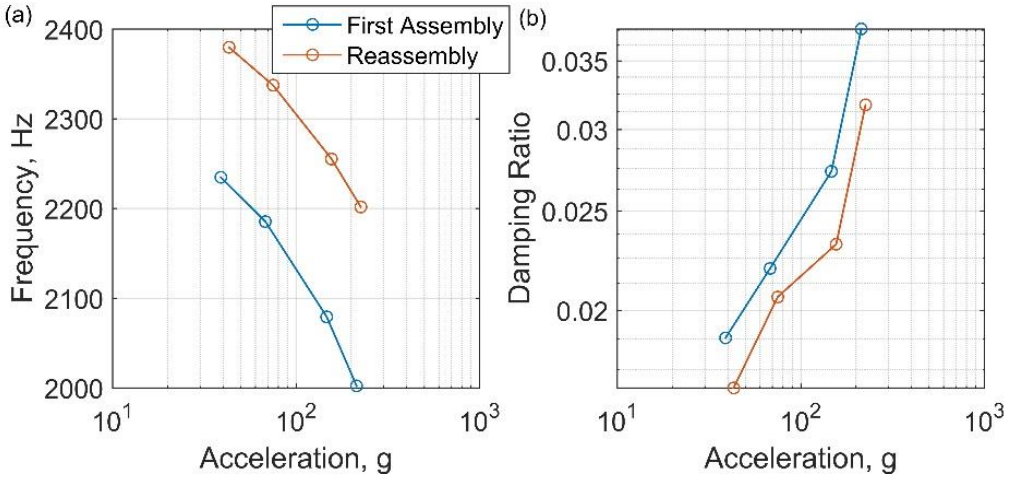

Figure 8. Amplitude dependent (left) resonant frequencies and (right) damping ratios estimated from swept sine tests for initial assembly and disassembly + reassembly.

4. MINISTACK ASSEMBLY MODELS

4.1. Solid Mechanics Finite Element Model

The Ministack geometry was meshed in Cubit using 406,720 first order hexahedral elements, otherwise referred to as HEX8 elements. The schematic in Figure 9 shows the finite element mesh used within Sierra/SM. The nodes at each interface between contiguous subcomponents align with one another but were unmerged to allow for the appropriate contact definition to be defined during simulation.

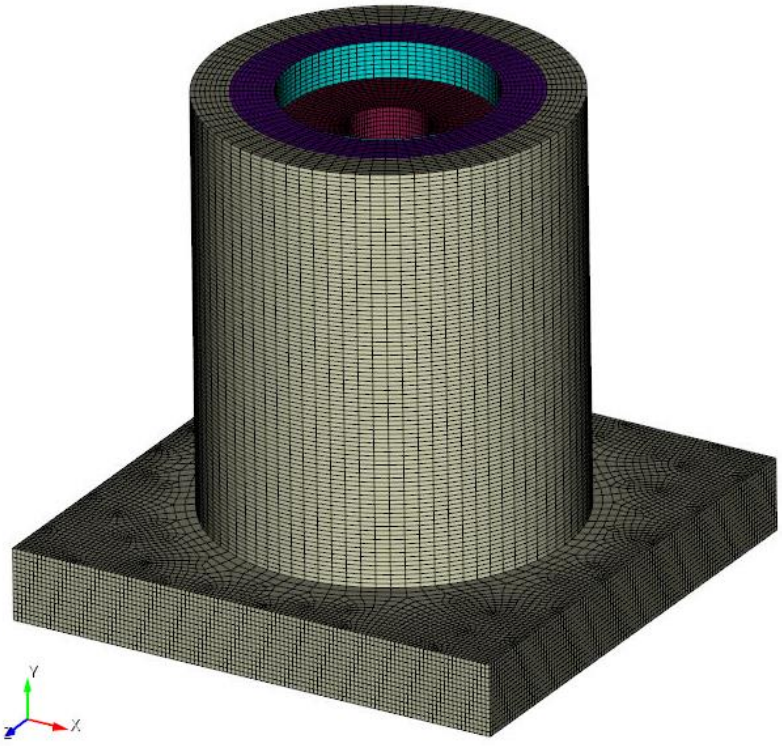

Figure 9. Finite element mesh of Ministack model.

The hexahedral elements model all the materials of each subcomponent (i.e. ring nut, cover plate, outer can, foam cups, slug) with linear elastic properties, as shown in Table 2. The model assumes that the foam cups behave as a linear elastic material, and that no viscous damping is added to account for material damping. The only source of energy dissipation within this model occurs when the frictional interfaces slip, making it easier to isolate and evaluate the damping mechanism. Frictional contact is defined between all blocks using the Dash search algorithm, augmented Lagrange enforcement, and face-face constraints. A Coulomb friction value of 0.4 is used at all interfaces denoted with black dashed lines in Figure 10. The implicit solver in Sierra/SM is used to gradually apply a preload as a distributed force to the top face of the retaining ring, which is then glued to the aluminum can once the preload level is reached. In Sierra/SM, glued constraints can be applied to deformed equilibrium states whereas tied constraints can only be applied to the undeformed configuration. The red dashed lines in Figure 10 show the locations of the glued constraint. The bottom of the can is fixed during application of preload and released once the preload is held in place. This preloaded state is used as the

initial equilibrium for all the dynamic simulations presented in this report. The explicit solver in Sierra/SM is used for all dynamic simulations.

Table *2*. Linear elastic material properties of Ministack.

Material	Component(s)	Young's Modulus	Density	Poisson's Ratio
Aluminum 6061-T6	Slug, Outer Can	68.9 GPa	2644 kg/m^3	0.33
Structural Steel	Ring Nut, Cover Plate	206.8 GPa	7800 kg/m^3	0.33
PMDI	Foam Cups	162 MPa	288.6 kg/m^3	0.30

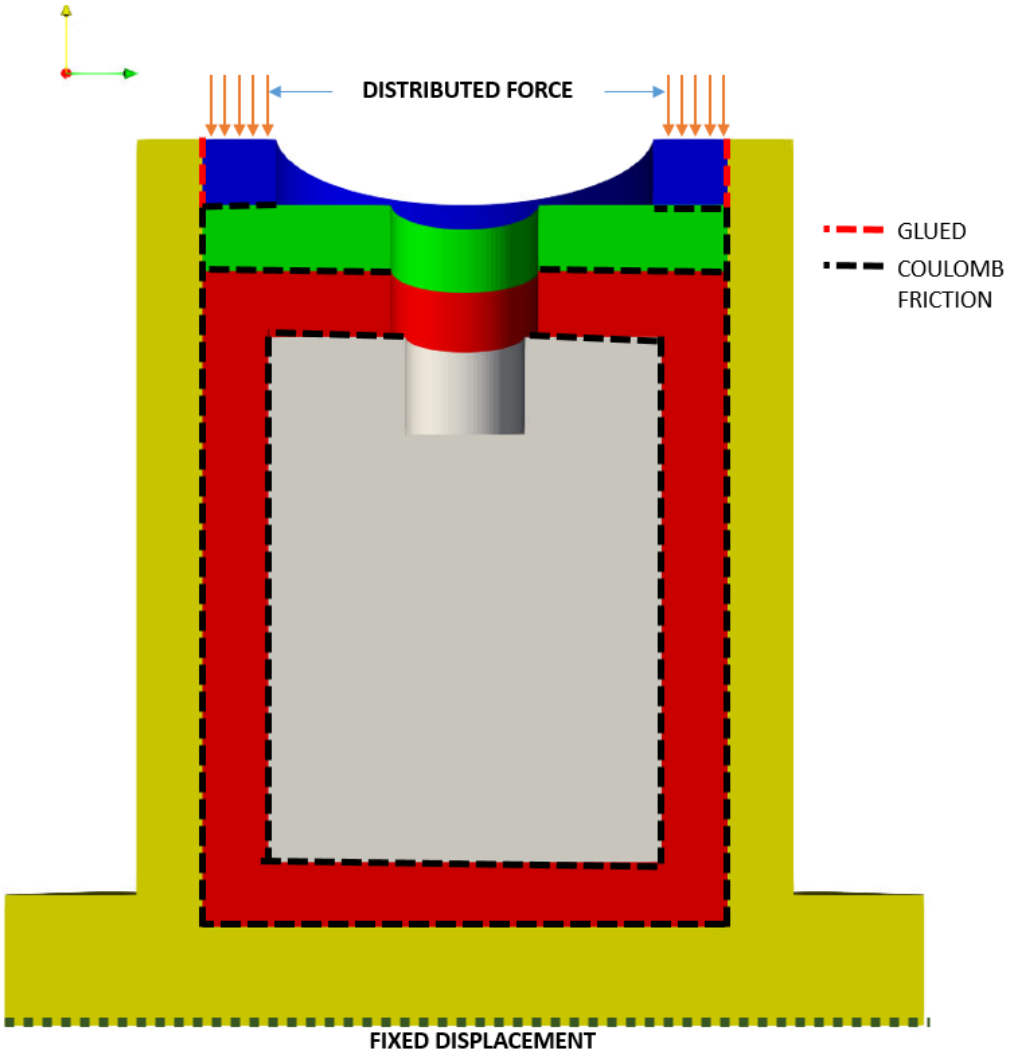

Figure 10. Boundary conditions in the Ministack model during preload.

4.2. Structural Dynamics Hurty/Craig-Bampton Model

A reduced order model was generated from the high fidelity finite element mesh developed in the previous subsection. In order to facilitate the reduced order model with whole joints representing the interface, rigid bar elements (known as RBAR in Sierra/SD [35]) constrain all the nodes on the radial slug-to-foam, and foam-to-can surfaces down to a single node at the center. A schematic of the mesh shown in Figure 11 shows the locations of these interfaces, and the spider node location to which each interface is rigidly constrained. These modeling decisions were informed through time simulations of the full fidelity model in Sierra/SM, as described in more detail in Section 5.1. The axial mode of interest exercises these two frictional interfaces during an impulsive load, and the top/bottom surfaces never lose preload within the excitation ranges input to the model.

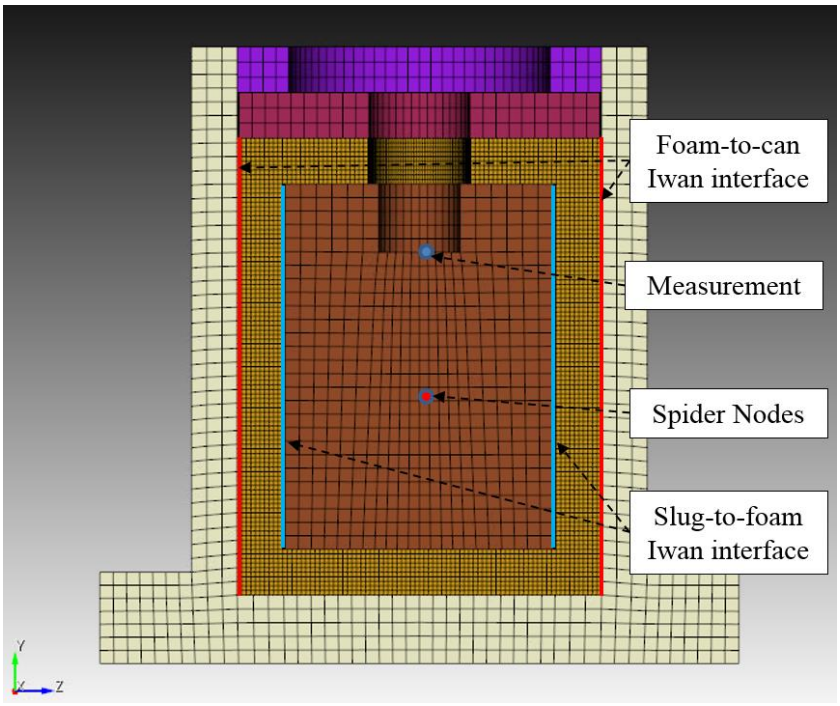

Figure 11. Ministack finite element model with MPC interfaces.

After constraining the four surfaces down to four independent spider nodes (all sharing the same physical location), the model was reduced using the Hurty/Craig-Bampton method as described in Section 2.2. A total of 25 fixed-interface modes describe the interior dynamics of the model, while 25 static constraint modes describe the static deflection due to a unit displacement of each interface DOF, which includes one physical DOF at the bottom surface of the can to apply base excitation. It is assumed that 25 is a sufficient number of fixed-interface modes since this captures modes up to 19 kHz, which is well beyond the frequency range of interest. The 50 DOF reduced order model is exported to MATLAB to facilitate the addition of Iwan and linear spring elements to define the interactions between the surfaces. Table 3 shows the directional elements connecting the two interfaces: four-parameter Iwan elements in the y-direction, and stiff elastic springs in all other directions. The drawback to using the Iwan element is that it is difficult to populate the parameters without fitting to experimental or simulated data. This issue is addressed later in Section 6 where an optimization procedure is developed to fit the Iwan parameters such that the amplitude

dependent frequency and damping of the solid mechanics model match those predicted from the whole joint reduced order model.

Table 3. Element definitions at HCB interfaces.

DOF	Element
X	Linear Spring
Y	Four-parameter Iwan
Z	Linear Spring
RX	Linear Spring
RY	Linear Spring
RZ	Linear Spring

5. NONLINEAR ENERGY DISSIPATION IN SIMULATION

5.1. Solid Mechanics Model

The high fidelity finite element model described in Section 4.1 is used to study the energy dissipation during dynamic excitation. An impulse was applied to the preloaded model in the form of a haversine in the axial y-direction to exercise the radial frictional interfaces. The shock simulation was performed using the explicit solver in Sierra/SM (also known as Presto) by applying the excitation to the bottom surface of the aluminum can. One of the most insightful observations from the Sierra/SM results was the amount of energy dissipated at two different interfaces. The model output both frictional energy dissipation (FED) and accumulated slip in order to inform the selection of interfaces to be modeled with a whole joint in the structural dynamics model described in Section 4.2.

Figure 12 shows these two metrics as a function of time resulting from the application of a 2 kHz haversine impulse with a 200 g amplitude. These plots show that the FED and slip of the foam/can and foam/slug radial interface increases immediately as the haversine is applied and flatlines around 15.004 seconds. Looking at the time history in the lowest subplot, it can be observed that the slug oscillates and decays during the first three or four cycles of response, and then reaches a steady state oscillation where no more energy dissipates from the response. The values of slip and FED also plateau at the same time that the velocity reaches steady state, meaning that the interfaces are stuck and no longer slipping. The accumulated slip is visualized on the finite element model in Figure 13 where the magnitude of the slip has been omitted since only qualitative comparisons between the different interfaces are of interest. The interfaces with the highest FED and slip (i.e. foam/can and foam/slug) were modeled using Iwan elements in the reduced structural dynamics model.

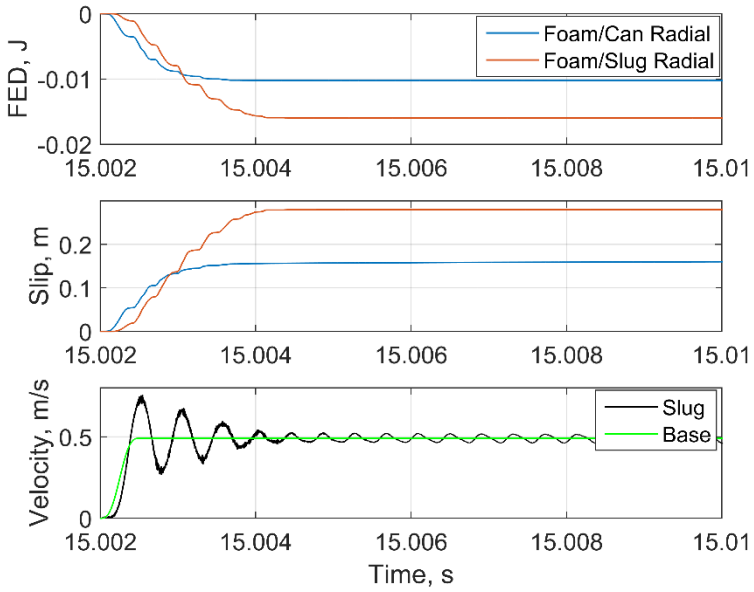

Figure 12. Response measured at various interfaces of the Ministack during shock excitation.

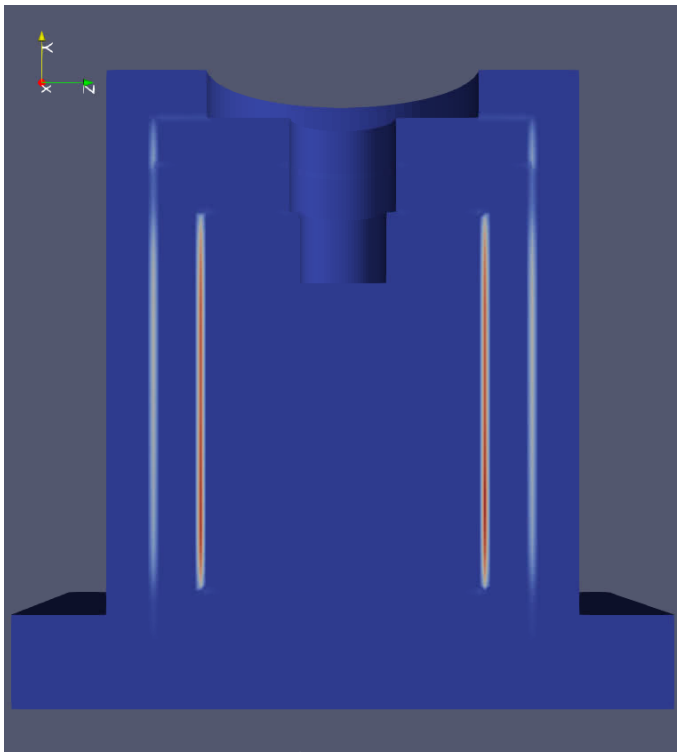

Figure 13. Accumulated slip after ring down.

Next, the 2 kHz haversine shock was applied at various peak amplitudes to extract the amplitude dependent frequency and damping from the ring-down response. This data was processed with the STFT and the curves are shown in Figure 14. The data shows a softening behavior in frequency which is expected since the interface is slipping at higher input levels. The data at the 350 g and 400 g loading shows that the frequency begins to plateau at high response amplitudes, while the damping starts to decrease, suggesting that the interfaces have reached macro-slip. Swept sine excitation was not applied to the solid mechanics model due to the computational cost associated with this approach. In addition, the authors are currently working to implement the quasi-static modal analysis approach using Sierra codes, so there are no results available at the time this document was written.

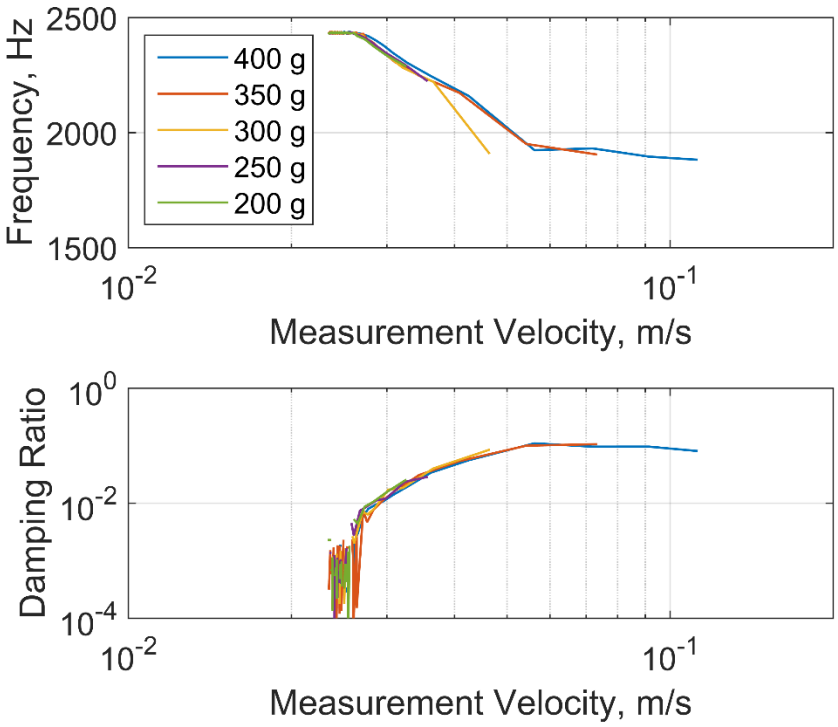

Figure 14. Amplitude dependent natural frequency (top) and damping ratio (bottom).

5.2. Structural Dynamics Reduced Order Model

The reduced order model of the Ministack with whole joint representations for the slug-to-foam and foam-to-can interface was simulated and evaluated using the three approaches discussed in Section 2.3, namely, transient ring-down processed with the STFT, swept sine response, and quasi-static modal analysis. The Iwan parameters used here are the assumed values given in Table 4 and have no expectation to match the behavior of the solid mechanics model. For the transient simulations (i.e. ring-down and swept sine), modal damping was added such that each mode possesses 0.5% critical damping. The transient and quasi-static simulations with the reduced order model resulted in a significant reduction in computational cost relative to the solid mechanics model since the model size goes from 1.34 million DOF down to only 50 DOF.

Table 4. Iwan element parameters for Ministack interfaces.

	Iwan Parameters			
	F_s *(N)*	K_T *(N/m)*	χ	β
Slug-to-Foam	1392	1.78×10^8	-0.65	0.004
Foam-to-Can	1392	1.78×10^8	-0.65	0.004

The first result for the reduced Ministack model shown in Figure 15 is the acceleration at the measurement location in Figure 11 in response to a haversine impulse with a frequency of 2 kHz

and base acceleration amplitude of 5000 g's. The input was applied in the y-axis, along the axis of the slug, in order to only excite the axial slug mode of the Ministack. On a single processor in MATLAB, the simulation took approximately 3.1 seconds to integrate over a 50 ms period. For computational cost comparison, the solid mechanics simulation took 8.5 hours to preload and apply the haversine impulse over 10 ms using 112 processors.

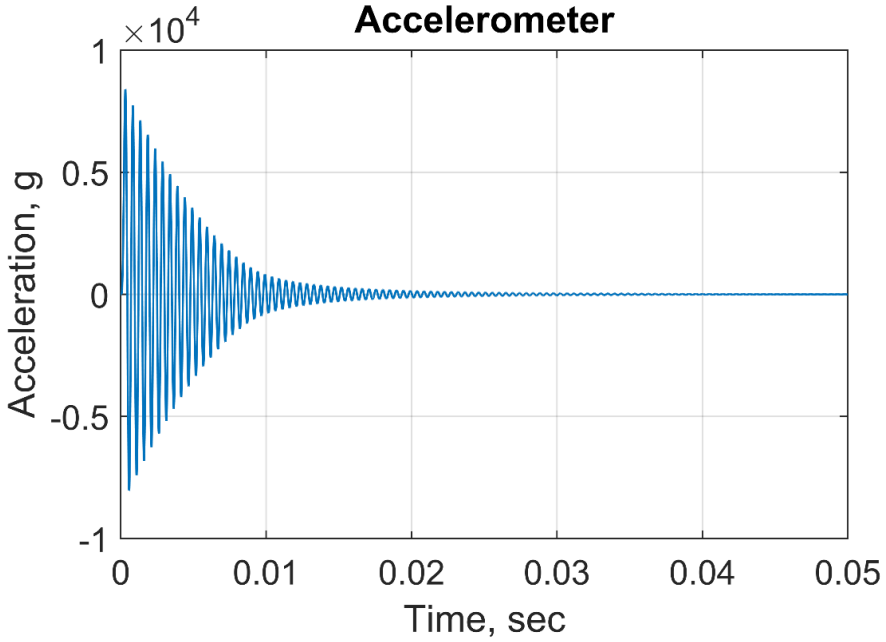

Figure 15. Ring-down y-axis acceleration of slug due to 2 kHz haversine impulse at 5000 g's.

The time history of the acceleration is processed with the STFT and the spectrogram of the signal is plotted in Figure 16. This figure directly reveals how the frequency content evolves with time. Notice that as the time increases, the amplitude of the response decays and the frequency *increases* until it remains constant throughout most of the signal. This frequency shift occurs quickly over a period of roughly 15 ms. From this STFT data, the amplitude dependent damping and frequency can be extracted following the approach in Section 2.3.1. The damping and frequency curves are plotted in Figure 17 against the acceleration amplitude at the measurement point. This data confirms the observations from the spectrogram, such that the frequency changes as a function of the acceleration amplitude. This shift is attributed to the loss in stiffness at the interface when the joint undergoes micro- and macro-slip. The change in effective damping also reveals that the slip at the interfaces dissipates energy at higher amplitudes due to frictional losses. As the response decays to low amplitudes, the frequencies and damping begin to converge towards the linear modal parameters: 2171 Hz natural frequency and 0.5% critical damping.

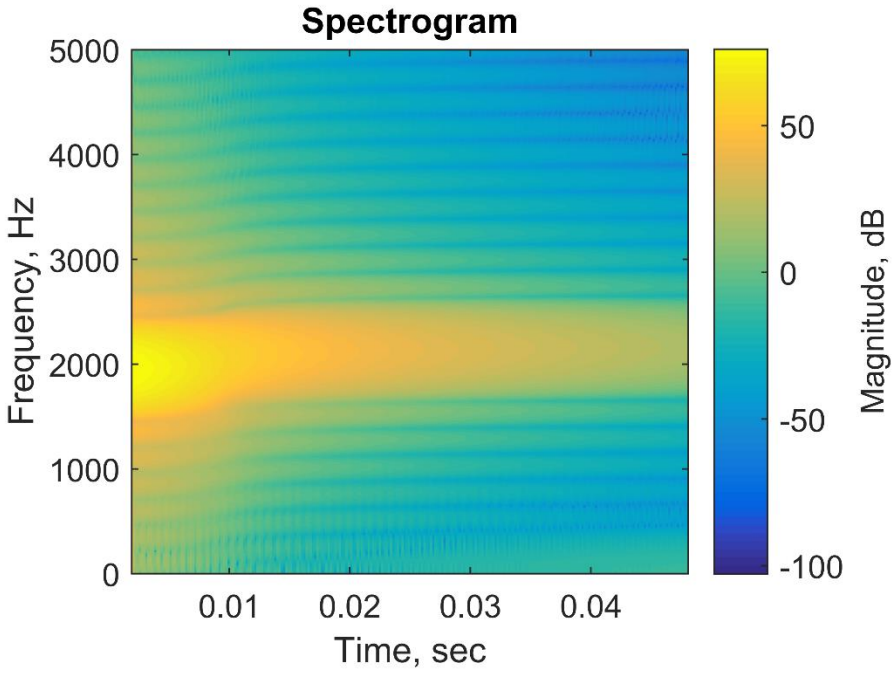

Figure 16. STFT spectrogram of slug ring-down acceleration.

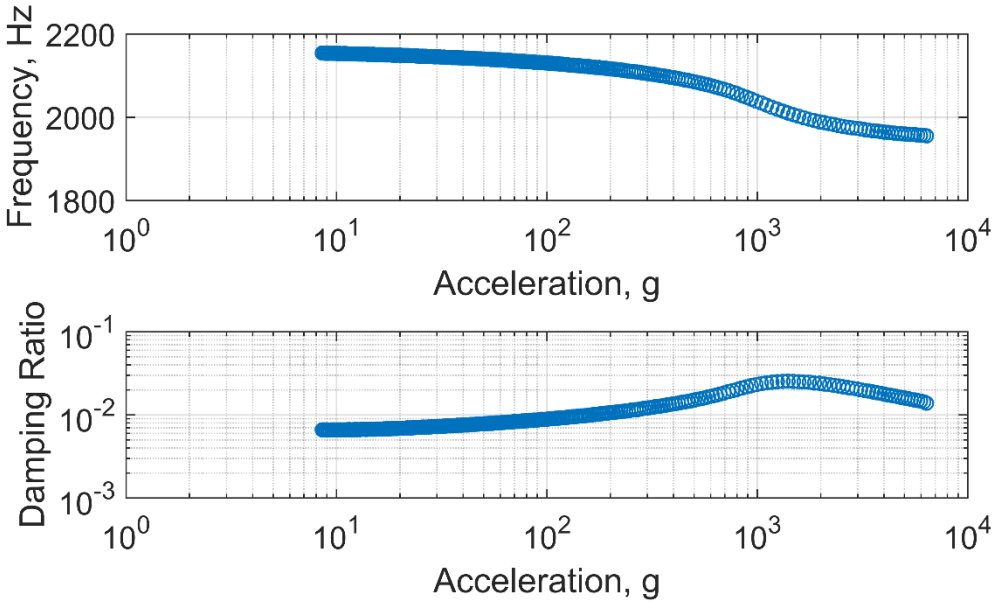

Figure 17. Amplitude-dependent natural frequency (top) and damping ratio (bottom) estimate using STFT from transient ring-down.

The transient ring-down response processed with the STFT algorithm provides tremendous insight into the nonlinear energy dissipation of the Ministack where frictional energy losses are important to capturing the damped response. While ring-down simulations only require a small period of response data, the method is only robust when it is feasible to excite a single mode of the structure. The Ministack has well separated modes in the axial direction, so it was possible to isolate this mode using a lower frequency haversine. Other input signals have been developed by

Pacini et al. [36] which could be used to isolate a single mode with a short duration input, although this was not explored in this report.

The alternative to impulsive loading is to excite the resonance of interest by applying swept sine excitations as discuss in Section 2.3.2. For the simulations applied to the reduced Ministack model, the frequency was swept from 1800 Hz to 2600 Hz over a period of 3.0 seconds, resulting in a sweep rate of 266.7 Hz/s. This rate was chosen to keep the computational cost within reason and shows to be sufficiently slow enough to capture the behavior of the system (as shown later in Figure 20). The sine sweeps were repeated for different base acceleration amplitudes, ranging from 0.00316 to 316 g's over a log scale. Each simulation in MATLAB (using the same integrator as before) required approximately 191 seconds of computer time to integrate the response. An example of the transfer function calculated from the highest amplitude input is shown in Figure 18. The location of the resonance determined by the phase lag between the input and output is marked with the black circle. Notice again that at high excitation levels, the peak frequency has shifted down as was seen with the transient ring-down response.

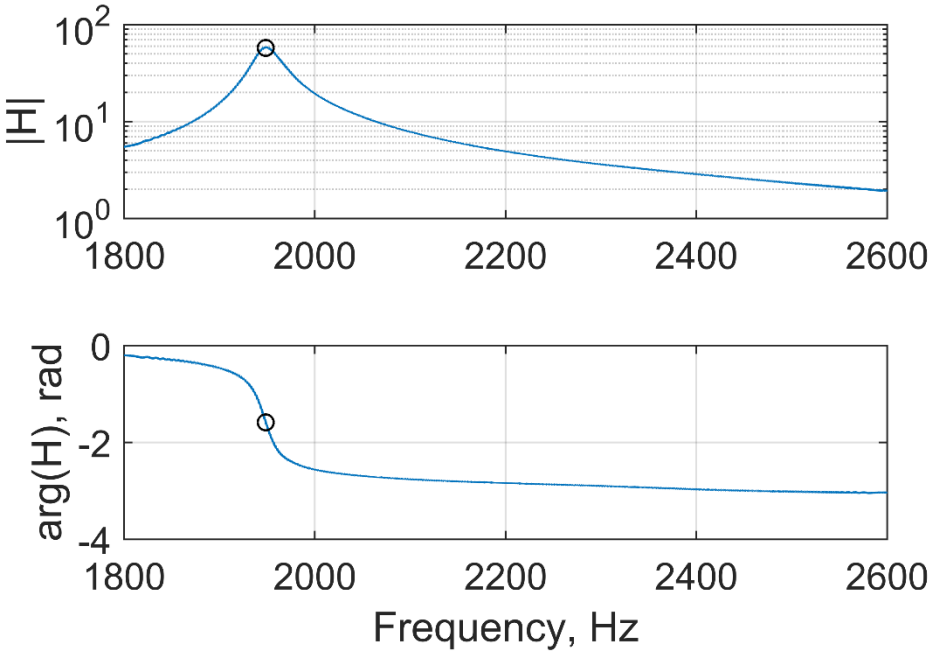

Figure 18. Magnitude (top) and phase (bottom) of the transfer function of a swept sine base acceleration with amplitude of 316 g's.

A total of 100 swept sine simulations were run to estimate the amplitude dependent frequency and damping shown in Figure 19. This resulted in roughly 5 hours of computational cost to extract essentially the same information from the ring-down data (which took 3 second to integrate). The advantage to swept sine excitations is that the sine sweep is capable of isolating a single mode of interest without coupling the excitation with other modes. In nonlinear systems, if a mode cannot be isolated by the input, then modal coupling can influence the post-processed amplitude dependent parameters (for example, see [17]). Sine sweeps are most commonly applied to experimental hardware and is rarely used for high fidelity modeling due to the length of simulation time required.

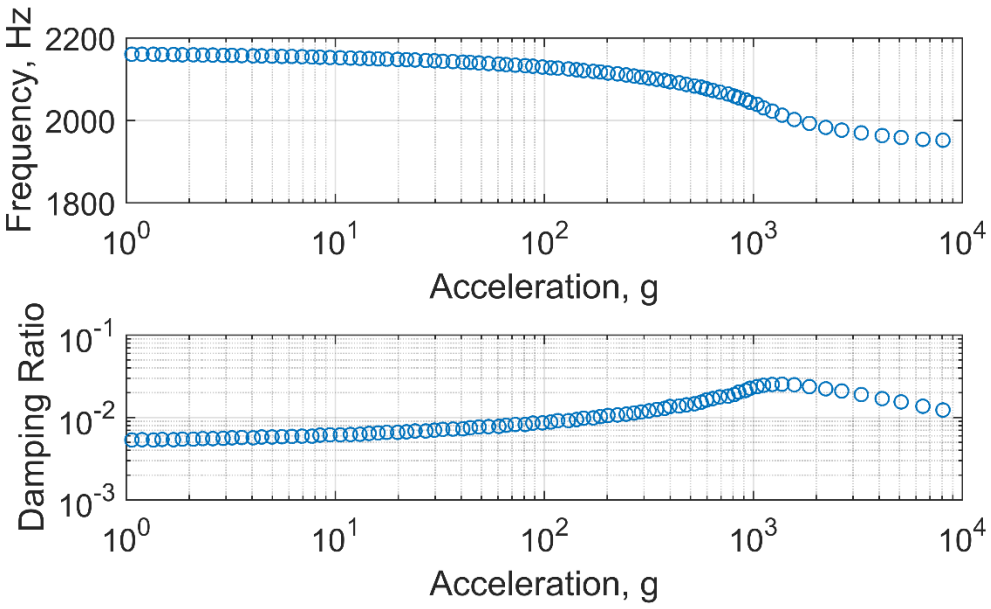

Figure 19. Amplitude-dependent natural frequency (top) and damping ratio (bottom) estimate from swept sine data.

The final method used to estimate the amplitude dependent modal parameters is the quasi-static modal analysis. The advantage to this approach is that only nonlinear static solutions are required from the model and it does not necessitate costly dynamic simulations over many time steps. The results from this approach are shown in Figure 20 in comparison to the STFT and swept sine data. The quasi-static modal analysis took 1.1 seconds to solve the deformation in response to 200 varying-amplitude force levels on a single processor in MATLAB. The results from all three approaches agree well with one another, suggesting that any of these can be used to estimate the amplitude dependent modal parameters for structures with mechanical interfaces.

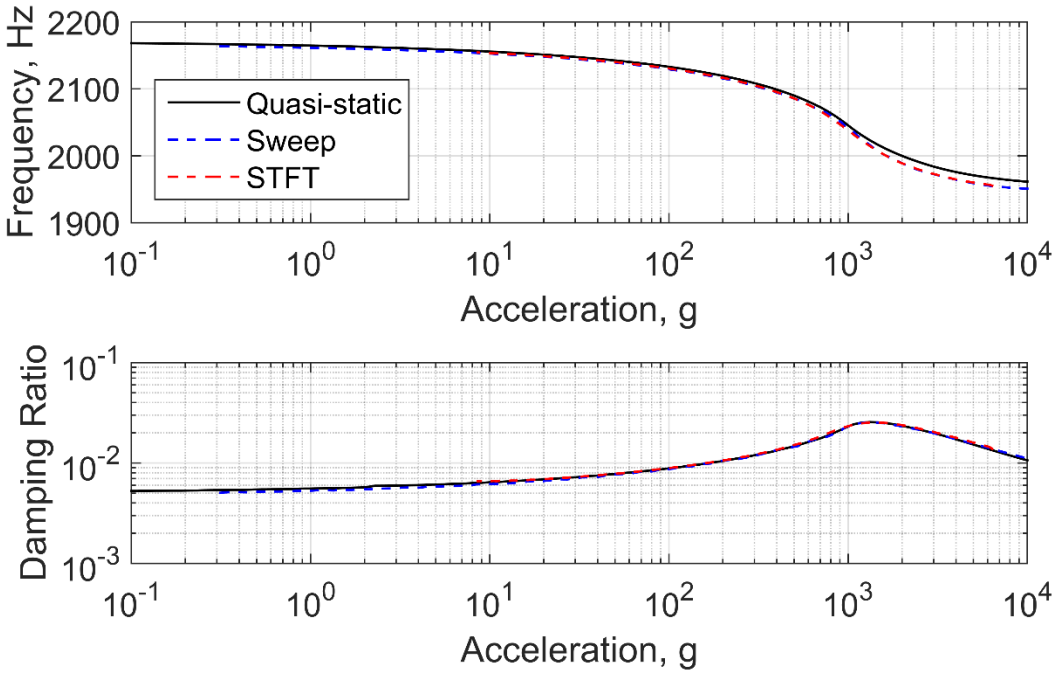

Figure 20. Comparison of amplitude-dependent natural frequency (top) and damping ratio (bottom) from STFT, swept sine, and quasi-static modal analysis.

6. MODEL CALIBRATION

6.1. Multi-Objective Optimization

The parameters of the Iwan element in the whole joint structural dynamics model are calibrated using multi-objective optimization with reference data generated from the solid mechanics model. The algorithm used in this report is the Non-dominated Sorting Genetic Algorithm II (NSGA-II), which is implemented in Python using the DEAP package [15]. NSGA-II was chosen because it has been shown to outperform other multi-objective optimization algorithms [37]. NSGA-II generates a random population of candidate solutions which are assigned a "fitness" based on whether they are considered being non-dominated or not. Non-domination is satisfied when there is no alternative solution with a better fitness in at least one of the objectives. The best candidates are chosen based on their fitness and recombined with other solutions. The set of best solutions from the original population and their offspring make it to the next generation and the process is repeated. NSGA-II pays special attention to "crowding distance" which is a measure of the uniformity of the spread of the Pareto-optimal front. The Pareto-optimal front is composed of all the non-dominated individuals in a population.

The multi-objective fitness function to be minimized is defined as,

$$\Gamma_{\mathrm{GA}} = \left(\sum_{i=1}^{N} \left(\frac{\omega_n(a_i) - \tilde{\omega}_n(a_i, \mathbf{p})}{\omega_n(a_i)} \right)^2, \frac{1}{N} \sum_{i=1}^{N} \left(\frac{\zeta(a_i) - \left(\tilde{\zeta}_{Iwan}(a_i, \mathbf{p})\right)}{\zeta(a_i)} \right)^2 \right) \tag{34}$$

Here the amplitude dependent natural frequencies, $\tilde{\omega}_n(a_i, \mathbf{p})$, and damping ratios $\tilde{\zeta}_{Iwan}(a_i, \mathbf{p})$, are computed from the quasi-static approach using the structural dynamics model for a set of unknown joint parameters, $\mathbf{p}$. The data from the solid mechanics model, $\omega_n(a_i)$ and $\zeta(a_i)$, are estimated from the STFT of the transient ring-down, as presented in Figure 14 in Section 5.1. The advantage to using the QSMA in the reduced model is the cost efficiency to evaluate one instance of the objective function. The other two dynamic time integrated solutions are more costly to simulate, and more difficult to automate within an optimization scheme.

6.2. Self-Calibration Study

An initial self-calibration study was performed to assess the ability of the optimizer to find a known set of parameters in the structural dynamics model. The Iwan parameters for the two interfaces were set to an arbitrary set of values, and the amplitude dependent frequency and damping ratio were extracted using QSMA. This data served as the reference data in the objective function, and the optimizer was used to best recover the known parameters. The known and optimized parameters from this study are shown in Table 5, and Figure 21 shows a normalized comparison of these two sets.

Table 5. Actual values of the Iwan elements parameters.

	Kt-1 (N/m)	Fs-1 (N)	Chi-1	Beta-1	Kt-2 (N/m)	Fs-2 (N)	Chi-2	Beta-2
Actual	1.78E+08	1390	-0.650	0.004	1.78E+08	1390	-0.650	0.004
Optimization	2.23E+08	1480	-0.707	0.0001	1.07E+08	1080	-0.523	0.007

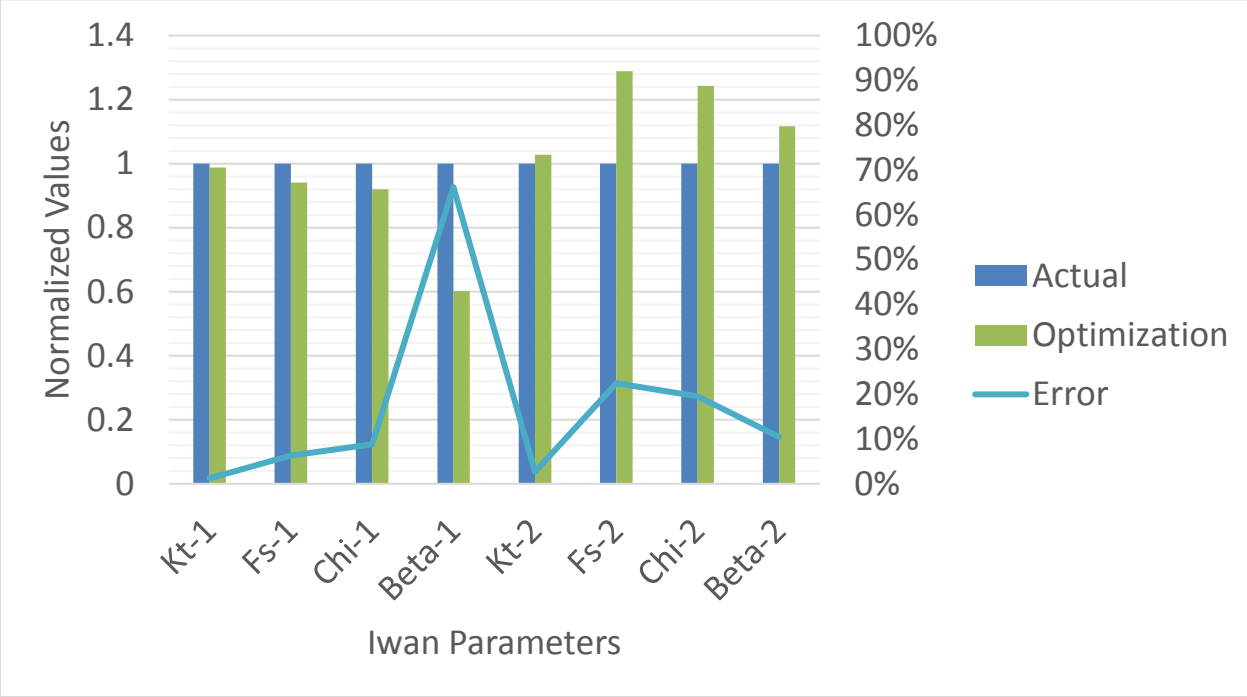

Figure 21. Normalized comparison of known and optimized parameters.

Although there were large differences between the known and optimized values of β and χ, the overall solution is in good agreement. The amplitude dependent frequency and damping with the optimized parameters were practically the same as the known parameters, as illustrated in Figure 22. This indicates that there are multiple equally acceptable solutions for different sets of parameters, as illustrated in the Pareto front in Figure 23, where the abscissa is the frequency objective and the ordinate is the damping objective. The red dot in the Pareto front figure represents the known solution. It is observed that the Pareto front does not match the known solution exactly, but there are many solutions that minimize the two objectives (frequency and damping). The valley between the front and the known solution could be an anomaly that is explained by the constraint resulting from each of the two Iwan elements having exactly the same parameters. Perturbing one of the Iwan elements causes the solution to fall within the Pareto found by the optimizer.

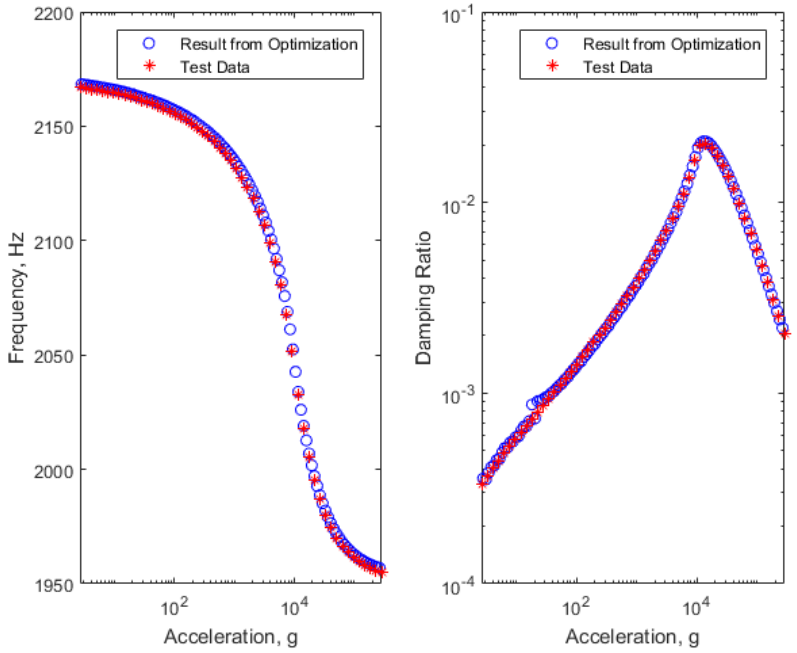

Figure 22. Comparison of the amplitude dependent frequency (left) and damping (right) using the known and optimized set of Iwan parameters.

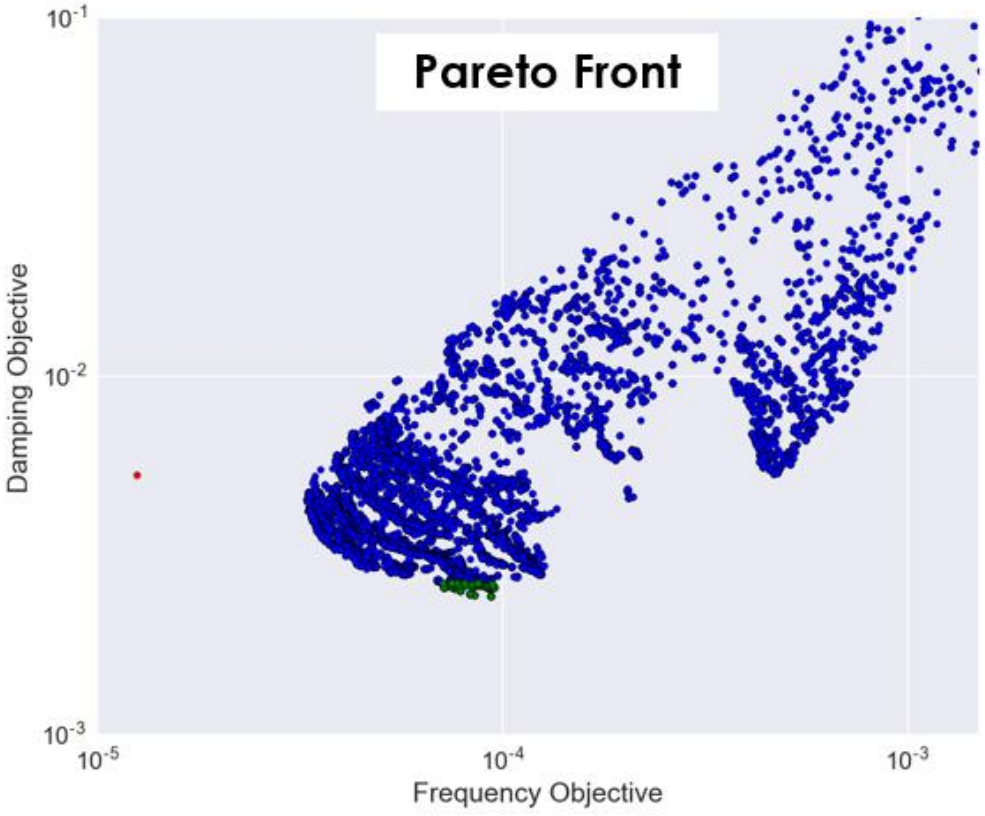

Figure 23. Pareto front generated by the NSGA-II solutions in blue and green. Known solution shown in red.

Another way of understanding the design space explored by the optimizer is to look at a self-organizing map (SOM). The SOM visualizes correlation and interactions between different parameters in high dimensional design spaces. The way to interpret a SOM is to look at the spatial distribution of color within a box. Each box represents a parameter, while the last two boxes represent the two objectives. The color represents the normalized magnitude of the parameters. As illustrated in Figure 24, the two objectives follow a very similar color distribution, indicating high correlation between them. The implication of this correlation is the existence of a global minimum because both objectives can be minimized simultaneously. Another useful feature that can be inferred from the SOM is the sensitivity of the objective to different parameters. It can be seen that F_s and K_T follow similar trends as the objectives and indicates that the objectives are highly sensitive to these parameters. However, β and χ follow different trends, which suggests low sensitivity to these parameters. This is consistent with the errors in Figure 21 that shows that, within a certain range, matching these parameters exactly is less important to match the amplitude dependent frequency and damping.

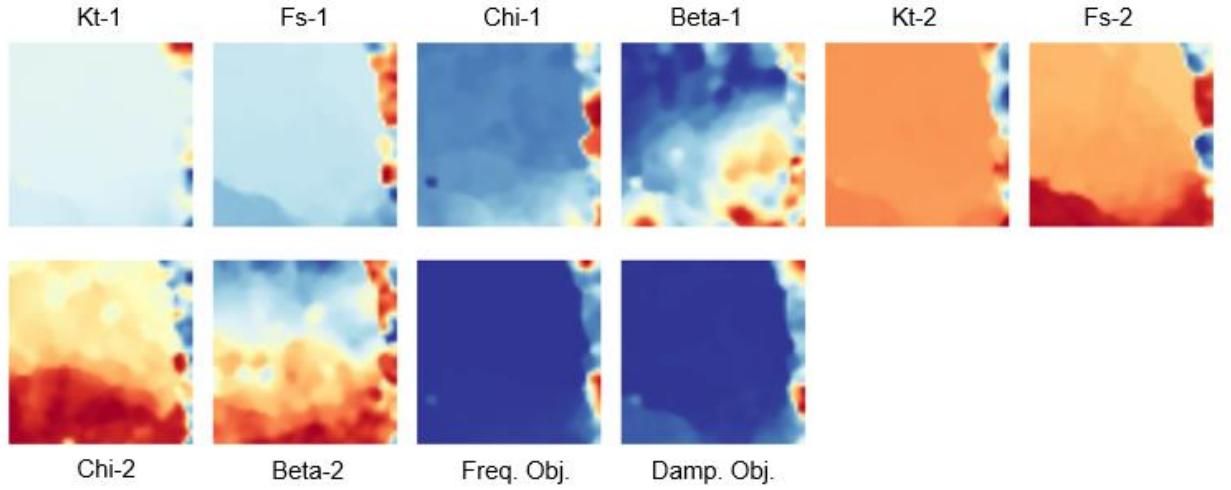

Figure 24. Self-organizing map showing correlations and interactions between design variables and objectives.

The optimized parameters show close agreement with the known values, although it is not able to exactly reproduce the values. In order to verify the results, the models with known and optimized Iwan parameters are simulated in response to a 2 kHz haversine input at various base acceleration amplitudes: 1, 10, 100, and 1000 g. The velocities at the measurement location are shown in Figure 25. At low amplitude response (i.e. 1 g input), the model behaves linearly and the slug oscillates with no energy dissipated over time. The amplitude and phase of the response agree over the entire period. For the nonlinear responses, the same observations are made such that the two models are in near perfect agreement. These results confirm that the slight discrepancies in Iwan element parameters have negligible effect on the simulated response.

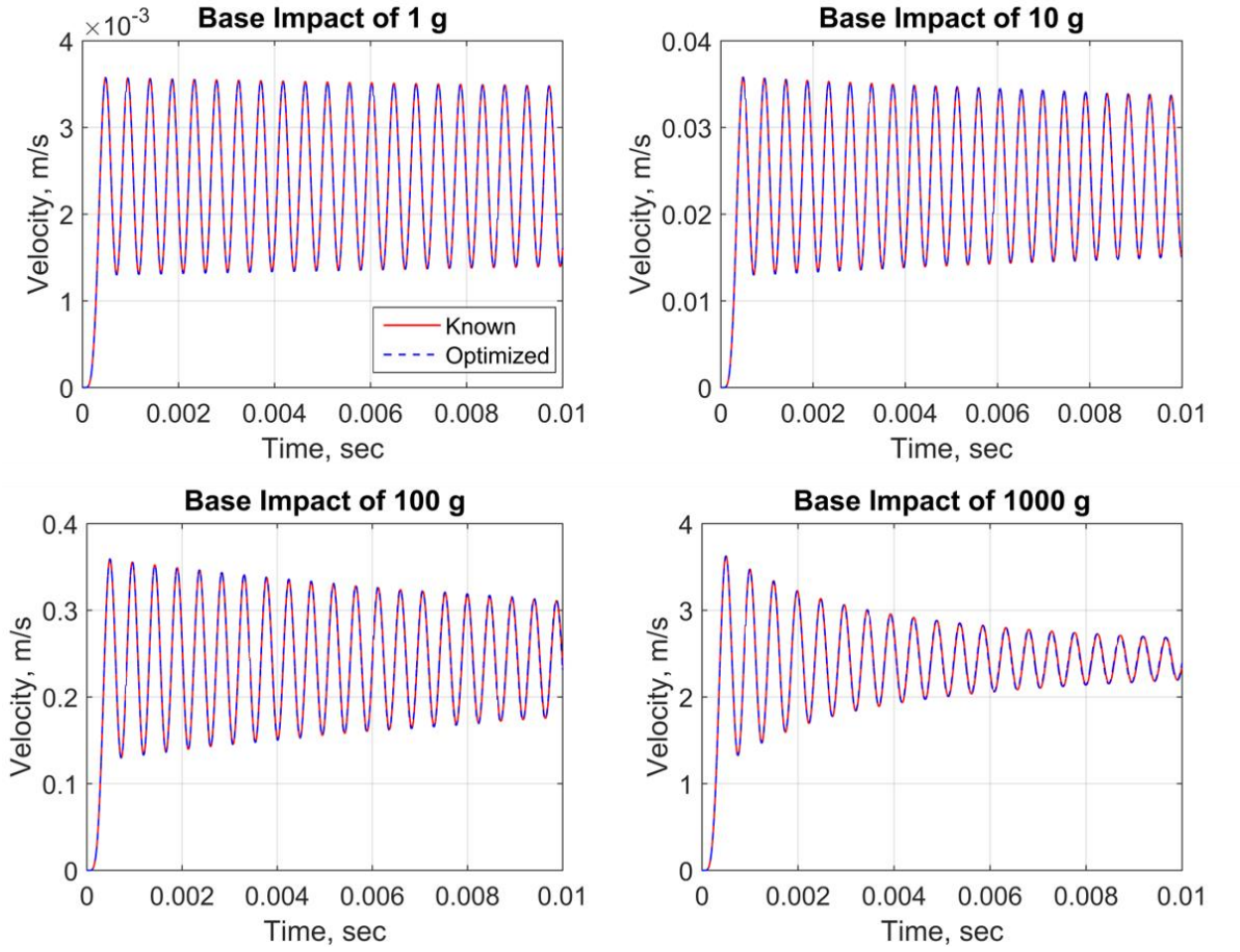

Figure 25. Time histories of transient ring-down simulated with structural dynamics model using known Iwan parameters (red) and optimized parameters (blue dashed).

6.3. Calibration with High Fidelity Model Data

Next, the response from the high fidelity solid mechanics model is used as the target data and the optimizer finds the set of Iwan parameters that are able to reproduce the behavior with the reduced order model. The target data was extracted from the response to the 2 kHz haversine base excitation with a 200 g amplitude. This amplitude was chosen to avoid macroslip behavior but still capture strong nonlinearities observed from microslip. The optimization results for amplitude dependent frequency and damping are shown in Figure 26. The black curves correspond to solutions in the Pareto-optimal front while the red curve is the target data. None of the solutions match the data both in frequency and damping simultaneously. In fact, the solutions are clustered into two groups based on the objective they are trying to match. This could be attributed to the presence of epistemic uncertainty in either the high fidelity model data or the reduced-order model. This is also evident in the way the Pareto front does not approach the origin in Figure 27.

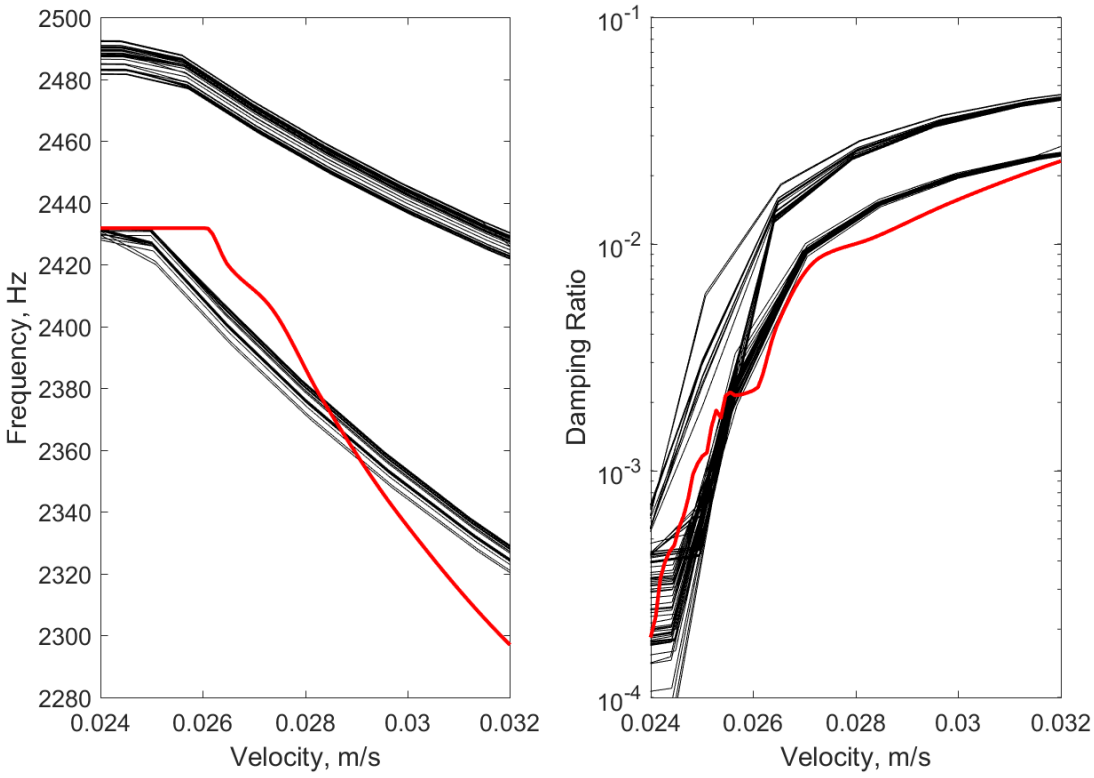

Figure 26. Comparison of the response using the known (red) and optimized set of Iwan parameters (black).

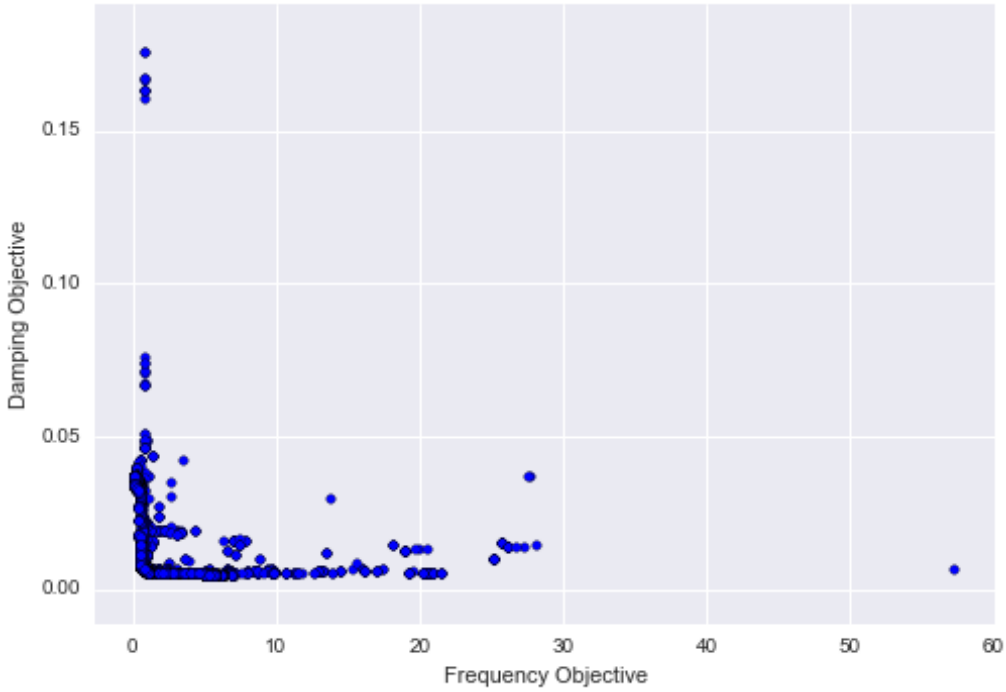

Figure 27. Pareto front generated by the NSGA-II solutions in blue.

The SOM also supports the possibility of epistemic uncertainty. As illustrated in Figure 28, the two objectives are not well correlated. This can be inferred from the way the color distributions diverge and as a consequence, they cannot be minimized simultaneously. This may be a symptom of inadequate friction modeling or a limitation of the four-parameter Iwan element.

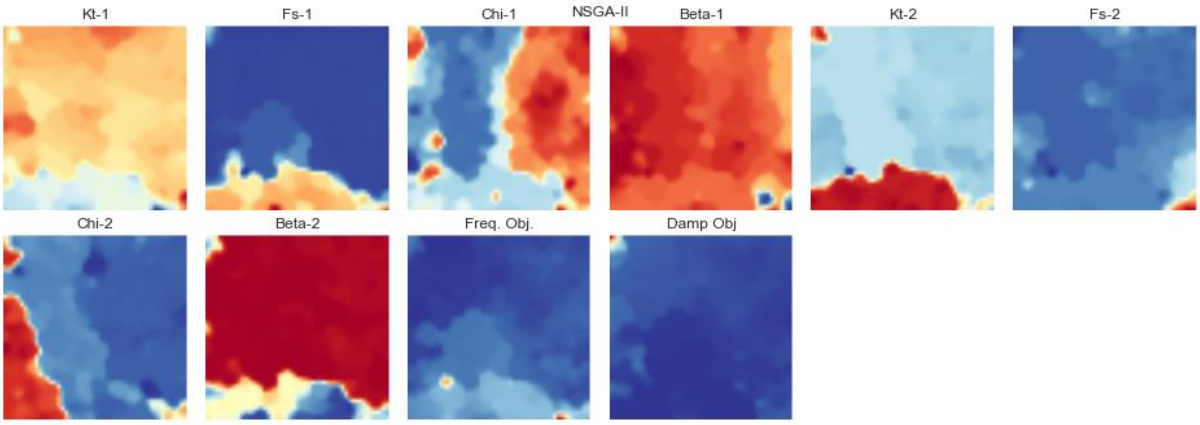

Figure 28. Self-organizing map showing correlations and interactions between design variables and objectives.

The time history response at the top of the slug is compared between the solid mechanics model and the calibrated reduced order model to a 2 kHz haversine input at various amplitudes to evaluate the level of discrepancy in the optimal solution. Since the optimizer did not find a set of parameters that matched both objectives simultaneously, the comparison for the reduced model optimized to the frequency objective is shown in Figure 29 while the optimal with respect to damping is in Figure 30. The frequency-matched results show fairly good agreement at low amplitude but the rate of frequency change at higher amplitudes disagrees with the solid mechanics model. The decay of the response at higher amplitude is not well captured either, which would be important for predicting the peak response amplitude during shock excitation. On the other hand, the model optimized to damping is inaccurate in terms of the phase (perhaps as expected), but overall the results are qualitatively better than the frequency-matched model. The rate of decay and peak response amplitude in the time domain is matched well. For predictive analysis, matching the peaks would be considered most valuable to obtain stress margins and acceleration levels. Overall, the calibrated reduced order model captures the dynamics from the solid mechanics model at a drastically reduced computational cost. For dynamic simulations requiring long periods of response, this slight sacrifice in accuracy seems to be significantly outweighed by the ability to predict responses in realistic timeframes.

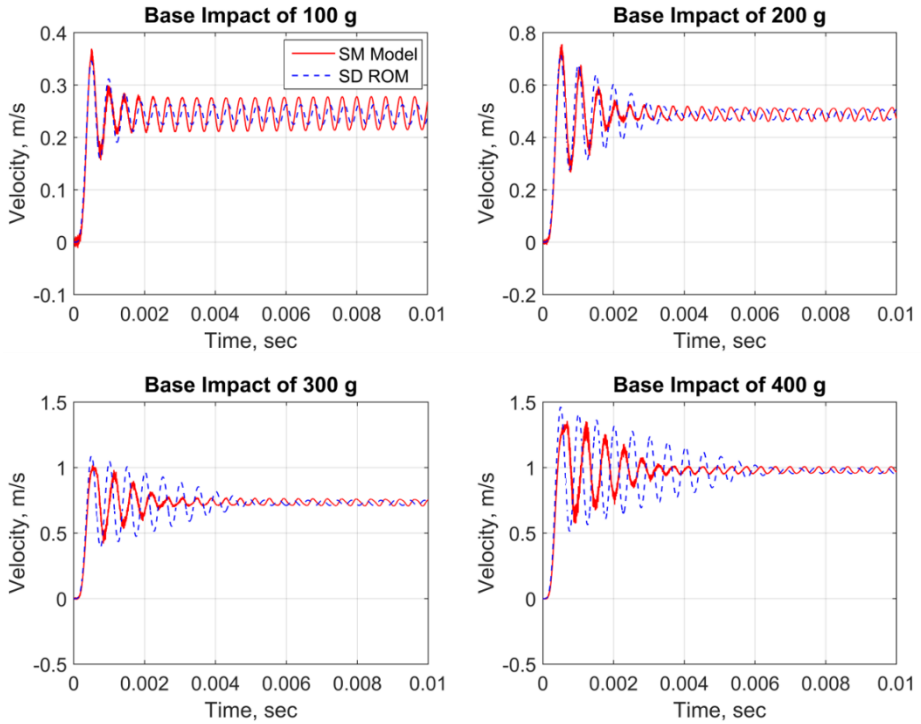

Figure 29. Time histories of transient ring-down simulated with (red) solid mechanics model and (blue dashed) reduced model optimized to frequency objective.

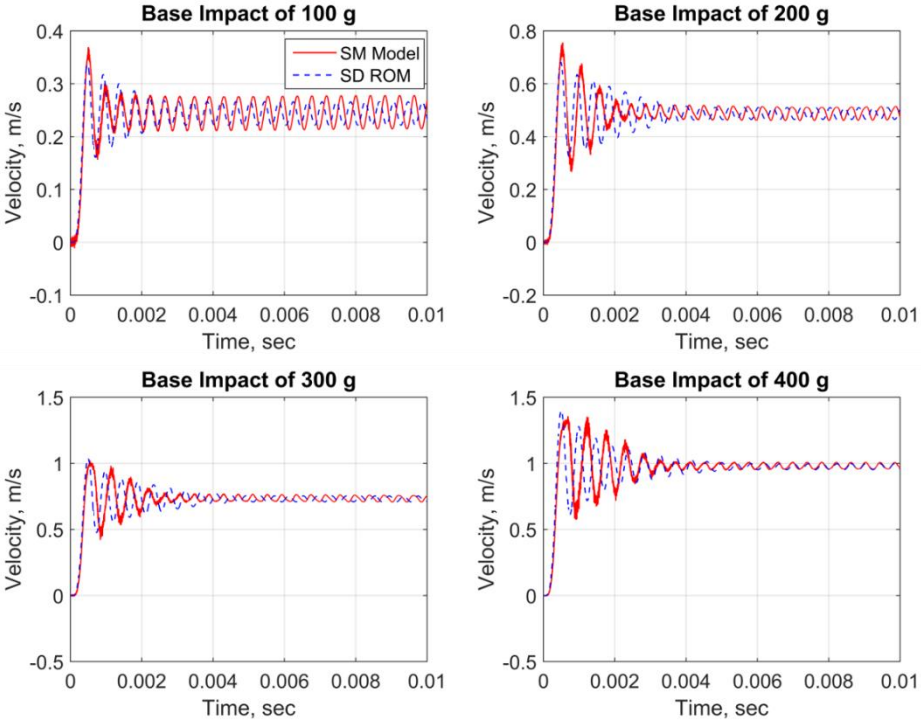

Figure 30. Time histories of transient ring-down simulated with (red) solid mechanics model and (blue dashed) reduced model optimized to damping objective.

7. CONCLUSION

The Ministack assembly finite element model is used to evaluate solid mechanics and structural dynamics modeling strategies to predict time history responses and amplitude dependent frequency and damping of nonlinear structures. This benchmark structure is assembled using a compression fit to maintain a preload on an internally packaged metal slug within foam encasement. The solid mechanics model developed in Sierra/SM models the physics at the interfacing surfaces using frictional contact, and is considered a high fidelity model. The structural dynamics model uses a reduced order Hurty/Craig-Bampton model to reduce the linear interior portion of the model with dynamic modes while retaining nonlinear degrees-of-freedom at the interface. The interface forces are modeled using a whole joint approach where the nodes on the surface are tied to a single point and connected via linear springs and four-parameter Iwan elements.

There are three different processing techniques that estimate the nonlinear amplitude dependent natural frequency and damping ratio of the finite element model. These are considered extensions of the linear modal parameters at low response levels. The first is a time-frequency analysis using the short-time Fourier transform to process transient ring-down response from impact excitation. This approach is amenable to modeling since only a short duration of simulation is required to extract the data but requires single mode isolation to be robust. The swept sine excitation uses traditional linear analyses to extract the damping and frequency at different response levels, but this generally requires many long time histories not readily obtained from high fidelity solid mechanics models. The quasi-static modal analysis solves the response of the model to a force proportional to the shape of a single mode, and estimates the frequency and damping from the modal displacement. This technique drastically reduces the computational cost since it only requires static solutions, therefore making it the ideal choice to use in model calibration and updating.

One of the drawbacks to using the structural dynamics modeling approach is that the Iwan elements are empirical and require calibration to fit the parameters that characterize a joint. A global multi-objective optimization scheme is developed to calibrate the Iwan parameters using amplitude dependent frequency and damping data obtained from the solid mechanics model. Simulation results from the solid mechanics model inform modeling decisions such as where to use whole joint models by analyzing the frictional energy dissipation and cumulative slip at interfaces in the Ministack. In the optimization algorithm, the reduced order model is sampled using quasi-static modal analysis to produce the amplitude dependent data due to its computational efficiency over comparable techniques. A self-calibration study shows that the NSGA-II algorithm is able to find optimal parameters that nearly match the known values. Verification of the optimal model with time simulations reveal that the calibrated model predicts responses to a high level of accuracy. When calibrating the structural dynamics model to the solid mechanics model, the amplitude dependent parameters did not match exactly. The damping and frequency could not be optimized simultaneously, likely due to epistemic uncertainty in the models. The simulated time response of the calibrated reduced order model matched the high fidelity data relatively well when the damping objective is emphasized in the optimization algorithm, suggesting that this is a feasible approach for predictive modeling that requires long response times.

A general methodology to model nonlinear structures with mechanical interfaces is reviewed in this report to highlight several recent advances in modeling and post-processing. The novel aspect developed here is the calibration of Iwan parameters to a high fidelity solid mechanics model using amplitude dependent frequency and damping estimated by quasi-static modal analysis. This technique is shown to be equivalent to other well-known methods and shows promise as a modeling workflow applicable to system and component level modeling work performed at Sandia National Laboratories. This workflow development will continue in the future by wrapping the quasi-static modal analysis algorithm around Sierra/SM and Sierra/SD to directly predict these curves from the high fidelity model for use in optimization, as well as other applications.

REFERENCES

[1] C. F. Beards, "Damping in structural joints," *The Shock and Vibration Digest,* vol. 24, pp. 3-7, 1992.

[2] L. Gaul and R. Nitsche, "The Role of Friction in Mechanical Joints," *Applied Mechanics Reviews,* vol. 54, pp. 93-106, 2001.

[3] S. Bograd, P. Reuss, A. Schmidt, L. Gaul, and M. Mayer, "Modeling the dynamics of mechanical joints," *Mechanical Systems and Signal Processing,* vol. 25, pp. 2801-2826, 2011.

[4] Sierra Solid Mechanics Team, "Sierra/SolidMechanics 4.42 User's Guide," SAND2016-9916 O, Sandia National Laboratories, Albuquerque, NM, October 2016.

[5] D. J. Segalman, "A Four-Parameter Iwan Model for Lap-Type Joints," *Journal of Applied Mechanics,* vol. 72, pp. 752-760, 2005.

[6] D. J. Segalman, D. L. Gregory, M. J. Starr, B. R. Resor, M. D. Jew, J. P. Lauffer, *et al.*, "Handbook on Dynamics of Jointed Structures," SAND2009-4164, Sandia National Laboratories, Albuquerque, NM, July 2009.

[7] Y. Li and Z. Hao, "A six-parameter Iwan model and its application," *Mechanical Systems and Signal Processing,* vol. 68–69, pp. 354-365, 2016.

[8] M. P. Mignolet, P. Song, and X. Q. Wang, "A stochastic Iwan-type model for joint behavior variability modeling," *Journal of Sound and Vibration,* vol. 349, pp. 289-298, 2015.

[9] R. Bouc, "Forced vibration of mechanical systems with hysteresis," presented at the Fourth Conference on Non-linear Oscillation, Prague, Czechoslovakia, 1967.

[10] Y.-K. Wen, "Method for random vibration of hysteretic systems," *Journal of the engineering mechanics division,* vol. 102, pp. 249-263, 1976.

[11] M. Oldfield, H. Ouyang, and J. E. Mottershead, "Simplified models of bolted joints under harmonic loading," *Computers & Structures,* vol. 84, pp. 25-33, 2005.

[12] A. E. Charalampakis and C. K. Dimou, "Identification of Bouc–Wen hysteretic systems using particle swarm optimization," *Computers & Structures,* vol. 88, pp. 1197-1205, 2010.

[13] A. E. Charalampakis and V. K. Koumousis, "Identification of Bouc–Wen hysteretic systems by a hybrid evolutionary algorithm," *Journal of Sound and Vibration,* vol. 314, pp. 571-585, 2008.

[14] Z.-C. Wang, Y. Xin, and W.-X. Ren, "Nonlinear structural joint model updating based on instantaneous characteristics of dynamic responses," *Mechanical Systems and Signal Processing,* vol. 76–77, pp. 476-496, 2016.

[15] F.-A. Fortin, F.-M. D. Rainville, M.-A. Gardner, M. Parizeau, and C. Gagné, "DEAP: Evolutionary algorithms made easy," *Journal of Machine Learning Research,* vol. 13, pp. 2171-2175, 2012.

[16] M. S. Allen, R. M. Lacayo, and M. R. W. Brake, "Quasi-static Modal Analysis based on Implicit Condensation for Structures with Nonlinear Joints," presented at the ISMA2016 - International Conference on Noise and Vibration Engineering, Leuven, Belgium, 2016.

[17] R. J. Kuether and M. R. W. Brake, "Instantaneous Frequency and Damping from Transient Ring-Down Data," in *Dynamics of Coupled Structures, Volume 4: Proceedings of the 34th IMAC, A Conference and Exposition on Structural Dynamics 2016,* M. Allen, R. L. Mayes, and D. Rixen, Eds., ed Cham: Springer International Publishing, 2016, pp. 253-263.

[18] B. J. Deaner, M. S. Allen, M. J. Starr, D. J. Segalman, and H. Sumali, "Application of Viscous and Iwan Modal Damping Models to Experimental Measurements From Bolted Structures," *Journal of Vibration and Acoustics,* vol. 137, 2015.

[19] M. Feldman, "Non-linear system vibration analysis using Hilbert transform--I. Free vibration analysis method'Freevib'," *Mechanical systems and signal processing,* vol. 8, pp. 119-127, 1994.
[20] J. M. Londoño, S. A. Neild, and J. E. Cooper, "Identification of backbone curves of nonlinear systems from resonance decay responses," *Journal of Sound and Vibration,* vol. 348, pp. 224-238, 2015.
[21] M. W. Sracic, M. S. Allen, and H. Sumali, "Identifying the modal properties of nonlinear structures using measured free response time histories from a scanning laser Doppler vibrometer," in *Topics in Nonlinear Dynamics, Volume 3*, Springer, 2012, pp. 269-286.
[22] H. Sumali and R. A. Kellogg, "Calculating damping from ring-down using Hilbert transform and curve fitting," in *4th International Operational Modal Analysis Conference (IOMAC), Istanbul, Turkey, May*, 2011, pp. 9-11.
[23] R. M. Lacayo, L. Pesaresi, J. Gross, D. Fochler, J. Armand, L. Salles, *et al.*, "Validation and Comparison of a Time Domain Approach and a Frequency Domain Approach for Nonlinear Modeling of Structures with Bolted Joints," *Mechanical Systems and Signal Processing (submitted),* 2017.
[24] M. Peeters, G. Kerschen, and J. C. Golinval, "Dynamic testing of nonlinear vibrating structures using nonlinear normal modes," *Journal of Sound and Vibration,* vol. 330, pp. 486-509, 2011.
[25] M. Peeters, G. Kerschen, and J. C. Golinval, "Modal testing of nonlinear vibrating structures based on nonlinear normal modes: Experimental demonstration," *Mechanical Systems and Signal Processing,* vol. 25, pp. 1227-1247, 2011.
[26] H. Festjens, G. Chevallier, and J.-l. Dion, "A numerical tool for the design of assembled structures under dynamic loads," *International Journal of Mechanical Sciences,* vol. 75, pp. 170-177, 2013.
[27] L. D. Jacobs-O'Malley and J. H. Hofer, "Nonlinear Feature Extraction and Energy Dissipation of Foam/Metal Interfaces," SAND2017-4293, Sandia National Laboratories, Albuquerque, NM, April 2017.
[28] J. Gross, J. Armand, R. M. Lacayo, P. Reuß, L. Salles, C. W. Schwingshackl, *et al.*, "A Numerical Round Robin for the Prediction of the Dynamics of Jointed Structures," presented at the 34th International Modal Analysis Conference (IMAC XXXIV), Orlando, Florida, 2016.
[29] R. R. J. Craig and M. C. C. Bampton, "Coupling of Substructures for Dynamic Analysis," *AIAA Journal,* vol. 6, pp. 1313-1319, 1968.
[30] W. C. Hurty, "Vibrations of structural systems by component mode synthesis," *Journal of the Engineering Mechanics Division,* vol. 86, pp. 51-70, 1960.
[31] G. Kerschen, M. Peeters, J. C. Golinval, and A. F. Vakakis, "Nonlinear normal modes. Part I. A useful framework for the structural dynamicist," *Mechanical Systems and Signal Processing,* vol. 23, pp. 170-94, 2009.
[32] S. W. Shaw and C. Pierre, "Normal Modes for Non-Linear Vibratory Systems," *Journal of Sound and Vibration,* vol. 164, pp. 85-124, 1993.
[33] A. F. Vakakis, "Non-linear normal modes (NNMs) and their applications in vibration theory: an overview," *Mechanical Systems and Signal Processing,* vol. 11, pp. 3-22, 1997.
[34] J. H. Ginsberg, *Mechanical and Structural Vibrations: Theory and Applications*, 1st ed., John Wiley and Sons, New York, 2001.

[35] Sierra Structural Dynamics Development Team, "Sierra Structural Dynamics-User's Notes," SAND2016-3046 O, Sandia National Laboratories, Albuquerque, NM, April 2016.
[36] B. R. Pacini, R. L. Mayes, B. C. Owens, and R. A. Schultz, "Nonlinear Finite Element Model Updating, Part I: Experimental Techniques and Nonlinear Modal Model Parameter Extraction," in *Dynamics of Coupled Structures, Volume 4: Proceedings of the 35th IMAC, A Conference and Exposition on Structural Dynamics 2017*, M. S. Allen, R. L. Mayes, and D. J. Rixen, Springer International Publishing, 2017, pp. 263-274.
[37] D. Kalyanmoy, S. Agrawal, A. Pratap, and T. Meyarivan, "A Fast Elitist Non-Dominated Sorting Genetic Algorithm for Multi-Objective Optimization: NSGA-II," in *International Conference on Parallel Problem Solving from Nature*, Paris, France, 2000, pp. 849-858.

DISTRIBUTION

1	MS0346	Diane Peebles	1556
1	MS0346	Mikhail Mesh	1553
1	MS0346	Adam Brink	1556
1	MS0346	Brett Robertson	1556
1	MS0346	Steven Gomez	1556
1	MS0346	Robert Kuether	1556
1	MS0386	Michael Starr	1557
1	MS0557	Charles Dennis Croessman	1520
1	MS0557	Benjamin Pacini	1522
1	MS0557	Daniel Roettgen	1522
1	MS0557	Kelsey Johnson	1521
1	MS0613	Laura Jacobs-O'Malley	2547
1	MS0825	Jeffrey Payne	1513
1	MS0840	James Redmond	1550
1	MS0899	Technical Library	9536 (electronic copy)


Sandia National Laboratories